CarbFix2: CO$_2$ and H$_2$S mineralization during 3.5 years of continuous injection into basaltic rocks at more than 250 °C

Deirdre E. Clark [a,*], Eric H. Oelkers [b,c], Ingvi Gunnarsson [d], Bergur Sigfússon [d], Sandra Ó. Snæbjörnsdóttir [d], Edda S. Aradóttir [d], Sigurður R. Gíslason [a]

[a] *Institute of Earth Sciences, University of Iceland, Reykjavík, Iceland*
[b] *Earth Sciences, University College London, London, United Kingdom*
[c] *Geosciences Environment Toulouse (GET), CNRS, UMR5563, Toulouse, France*
[d] *Reykjavík Energy, Reykjavík, Iceland*

Abstract

The CarbFix method was upscaled at the Hellisheiði geothermal power plant to inject and mineralize the plant's CO$_2$ and H$_2$S emissions in June 2014. This approach first captures the gases by their dissolution in water, and the resulting gas-charged water is injected into subsurface basalts. The dissolved CO$_2$ and H$_2$S then react with the basaltic rocks liberating divalent cations, Ca^{2+}, Mg^{2+}, and Fe^{2+}, increasing the fluid pH, and precipitating stable carbonate and sulfide minerals. By the end of 2017, 23,200 metric tons of CO$_2$ and 11,800 metric tons of H$_2$S had been injected to a depth of 750 m into fractured, hydrothermally altered basalts at >250 °C. The *in situ* fluid composition, as well as saturation indices and predominance diagrams of relevant secondary minerals at the injection and monitoring wells, indicate that sulfide precipitation is not limited by the availability of Fe or by the consumption of Fe by other secondary minerals; Ca release from the reservoir rocks to the fluid phase, however, is potentially the limiting factor for calcite precipitation, although dolomite and thus aqueous Mg may also play a role in the mineralization of the injected carbon.

During the first phase of the CarbFix2 injection (June 2014 to July 2016) over 50% of injected carbon and 76% of sulfur mineralized within four to nine months, but these percentages increased four months after the amount of injected gas was doubled during the second phase of CarbFix2 (July 2016 – December 2017) at over 60% of carbon and over 85% of sulfur. The doubling of the gas injection rate decreased the pH of the injection water liberating more cations for gas mineralization. Notably, the injectivity of the injection well has remained stable throughout the study period confirming that the host rock permeability has been essentially unaffected by 3.5 years of mineralization reactions. Lastly, although the mineralization reactions are accelerated by the high temperatures (>250 °C), this is the upper temperature limit for carbon storage via the mineral carbonation of basalts as higher temperatures leads to potential decarbonation reactions.
© 2020 The Author(s). Published by Elsevier Ltd. This is an open access article under the CC BY-NC-ND license (http://creativecommons.org/licenses/by-nc-nd/4.0/).

Keywords: CCS; CO$_2$; H$_2$S; Basalt; Mineral storage; Gas mixtures; CarbFix

1. INTRODUCTION

Upon the successful rapid subsurface mineral storage of carbon and sulfur at the original CarbFix site (Matter et al., 2016; Snæbjörnsdóttir et al., 2017), the CarbFix method was upscaled at the Hellisheiði geothermal power plant,

---

which emits about 41,000 metric tons of CO_2 and 10,000 metric tons of H_2S annually as a by-product of geothermal energy production (Gunnarsson et al., 2018). Icelandic regulations, stricter than WHO guidelines, have been in effect to cut down H_2S emissions of the geothermal industry since 2010 (Aradóttir et al., 2015). These regulations motivated the development of H_2S abatement techniques by mineral storage (Aradóttir et al., 2015; Gunnarsson et al., 2015a), in conjunction with carbon mineralization, the latter deemed the safest way of storing carbon in the subsurface (Benson and Cook, 2005; Gislason and Oelkers, 2014; McGrail et al., 2006). By combining these efforts, a mixed CO_2–H_2S gas injection has been pursued at Hellisheiði to reduce both the CO_2 and H_2S emissions of the power plant, with the advantage of significantly decreasing the cost of their capture and storage (Aradóttir et al., 2015; Gunnarsson et al., 2018).

The CarbFix method first captures CO_2 and H_2S in water either during its injection (Gislason and Oelkers, 2014; Sigfusson et al., 2015) or in a scrubbing tower adjacent to the gas source (Gunnarsson et al., 2018). The resulting gas-charged injection water is acidic. Upon its injection into basalts, this acidic water accelerates the dissolution of the basaltic rocks releasing divalent cations, Ca^{2+}, Mg^{2+}, and Fe^{2+}, to the injected waters. These cations react with the dissolved CO_2 and H_2S to form stable carbonate and sulfide minerals (Gislason and Oelkers, 2014; Power et al, 2013; Stefánsson et al., 2011). From January to August 2012, 175 metric tons of pure CO_2 and 73 metric tons of a gas mixture (75% CO_2 – 24% H_2S – 1% H_2) were injected into basaltic rocks at the original CarbFix site in Iceland, having a temperature of 20–50 °C. This pilot study demonstrated that 95% of the CO_2 was mineralized in less than two years predominantly as calcite and essentially all of the H_2S within four months as pyrite (Matter et al., 2016; Oelkers et al., 2019a, 2019b; Pogge von Strandmann et al., 2019; Snæbjörnsdóttir et al., 2017). In a different effort, 1000 tons of supercritical CO_2 was injected into Columbia River Basalts during July – August 2013 at the Wallula Basalt pilot site, USA. Results validated carbonate mineralization with both calcite and ankerite identified in sidewall core samples extracted from the injection zone two years post-injection (McGrail et al., 2017a, 2017b). Research has also begun to evaluate the feasibility of collecting and storing 50 million metric tons of CO_2 in basalt formations offshore from Washington, USA and British Columbia, Canada (Goldberg et al., 2018).

The CarbFix2 project upscaled the original CarbFix project by capturing and injecting a portion of the CO_2 and H_2S emissions of the Hellisheiði geothermal power plant into geothermally altered basalts at temperatures of ~260 °C beginning in June 2014. By the end of 2017, 23,200 metric tons of CO_2 and 11,800 metric tons of H_2S had been injected to a depth of 750 m. Four previous reports of this mixed gas injection in Iceland have been published thus far: (1) a detailed description of the injection method and the monitoring of the dissolved CO_2 and H_2S in the wells downstream from the injection well until 2015 by Gunnarsson et al. (2018), (2) an account of the mixed gas capture method by Sigfússon et al. (2018), (3) geochem-

ical data from the injection well by Clark et al. (2018), and (4) a description of the hydrology and the alteration of the rocks before the CarbFix2 injection by Snæbjörnsdóttir et al. (2018b).

This study expands the geochemical monitoring data originally presented by Gunnarsson et al. (2018) by extending the previously reported measured concentrations and mass balance calculations of dissolved inorganic carbon (DIC) and dissolved sulfur by two years (2016–2017), and presenting the major element (Al, Na, K, Cl, F, B) and cation (Ca, Mg, Fe) concentrations of fluid collected from three monitoring wells from the start of the CO_2–H_2S injection in 2014 until the end of 2017. Mass balance calculations, mineral saturation indices, and predominance diagrams of primary and secondary minerals (e.g. carbonates, sulfides, epidote) in these fluids were then generated from these results using a revised thermodynamic database by Voigt et al. (2018a). This expanded chemical dataset allows assessment of the magnitude of carbon and sulfur mineralization in the subsurface in relation to other relevant primary and secondary minerals in the target basaltic reservoir.

2. THE CARBFIX2 PROJECT

The CarbFix2 injection site (Fig. 1) is located 1.5 km north of the Hellisheiði geothermal power plant in Húsmúli, a part of the southern Hengill volcanic system that consists of fractured, hydrothermally altered basalts. Studies of the Hellisheiði geothermal field reveal sequences of alteration mineral assemblages as a function of increased depth and temperature (Franzson et al., 2010; 2005). The alteration phases of the original CarbFix site, located about two km southwest of the power plant at a depth of 500 m and a temperature of 20–50 °C, were chalcedony, smectites, calcite, and Ca-rich and Na-rich zeolites (Alfredsson et al., 2013). The main aquifer of the CarbFix2 storage site, however, is located below the end of the cased section of the injection well at depths greater than 1300 m with temperatures of >250 °C. At these conditions, the major alteration minerals are chlorite, epidote, and prehnite. Actinolite is anticipated at temperatures around 280 °C. Other commonly observed secondary minerals at the CarbFix2 site include wollastonite, wairakite, albite, calcite, pyrite, and pyrrhotite. In addition, quartz rather than chalcedony is present at >180 °C (Snæbjörnsdóttir et al., 2018b). It is important to highlight that geothermal systems are characterized by their hydrothermal convection. Fluid circulation is essentially density-driven when temperatures at the base of the circulation are above ~150 °C. Therefore as primary geothermal fluids rise towards the surface, the formation of secondary geothermal fluids occurs due to fluid phase segregation and fluid mixing with shallower and cooler groundwater (Arnorsson et al., 2007).

There have been two distinct phases of gas injection in CarbFix2, as described in more detail by Clark et al. (2018) and Sigfússon et al. (2018). During the first phase, effective from 23 June 2014 to 15 July 2016, approximately 25% of the exhaust gas of the powerplant comprised of 63 vol% CO_2, 21 vol% H_2S, 14 vol% H_2, and 2 vol% of other
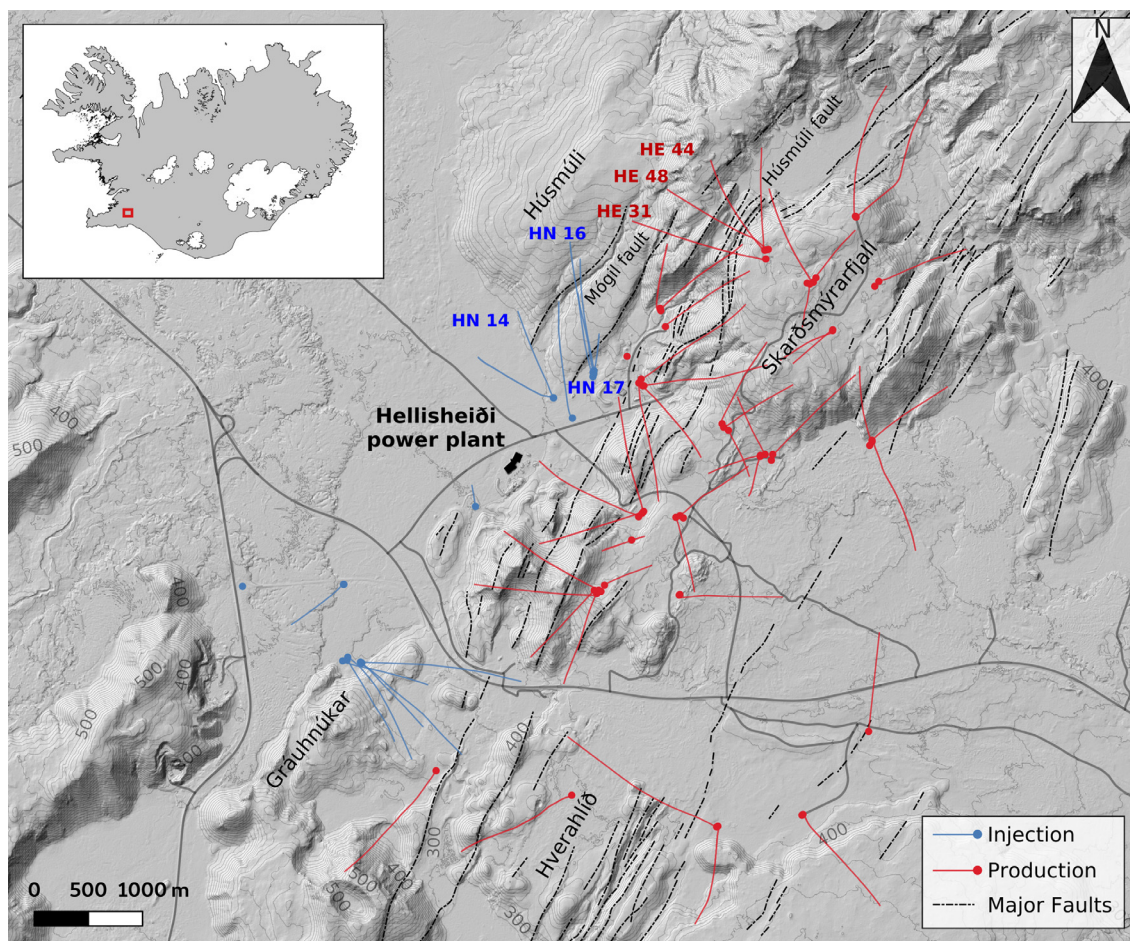
Fig. 1. An overview of the CarbFix2 injection site. The gas separation plant is located at the Hellisheiði power plant in the center of the figure. A 1.5 km long, gas-charged water pipe connects the gas capture plant to the injection wells. Injection was into wells HN-16 and HN-14, which are directionally drilled as shown by the line from the surface location. The three monitoring wells (HE-31, HE-48, and HE-44), also directionally drilled, are located from one to two km down gradient from the injection well.

gases, predominantly Ar, CH_4, and N_2, was dissolved into 20 °C condensate (condensed steam from the power plant turbines) in a single step in a scrubbing tower at 5 bar pressure and 30–36 l/s. The CO_2 and H_2S charged condensate water was then pressurized to 9 bar and transported 1.5 km to injection wells HN-16 or HN-14 (Gunnarsson et al., 2018). Due to unrelated repairs to an inner pipe in injection well HN-16, gas injection was switched to HN-14 from 15 July 2015 to 15 March 2016. From 15 July 2016, the scrubbing tower gas capture capacity was doubled with the pressure raised to 6 bar and its resulting gas-charged condensate water was pressurized to 9 bar and subsequently injected into well HN-16. This injection well is directionally drilled, as shown in Fig. 1, 2204 m long, and 0.311 m wide with the top 660 m encased in carbon steel; HN-14 is of similar design at 2039 m in length with the top 690 m encased. Effluent water is injected into the wells at a rate of 15–130 l/s. The gas-charged condensate water from the scrubbing tower was injected separately into a 4″ stainless steel pipe within the carbon steel casing at a rate

of 30–60 l/s (Fig. 2). Injection well flow rates are a function of the temperature, pressure, and the amount of water injected into other injection wells in the vicinity; injection rates during this study are shown in Fig. 2. Despite minor variations, the injection flow rates have not decreased with time and the injection pressure has remained close to constant, indicating that the permeability of the system has not degraded over the 3.5 year study period. The flow rates of both injection wells as well as the operation status of the gas capture compressors from 2014 to 2017 are reported in Sigfússon et al. (2018); note that pure condensate water flow in HN-16 began on 22 April 2014 before the gas capture plant was in operation two months later. The gas-charged condensate water takes two to four minutes to reach the end of this stainless steel pipe within the injection wells, and then mixes with the effluent water while taking an additional 10–45 min to reach high permeability fractures at depths below 1300 m. Three geothermal production wells, HE-31, HE-48, and HE-44 (Fig. 1), were used as monitoring wells. These wells are located 984, 1356, and
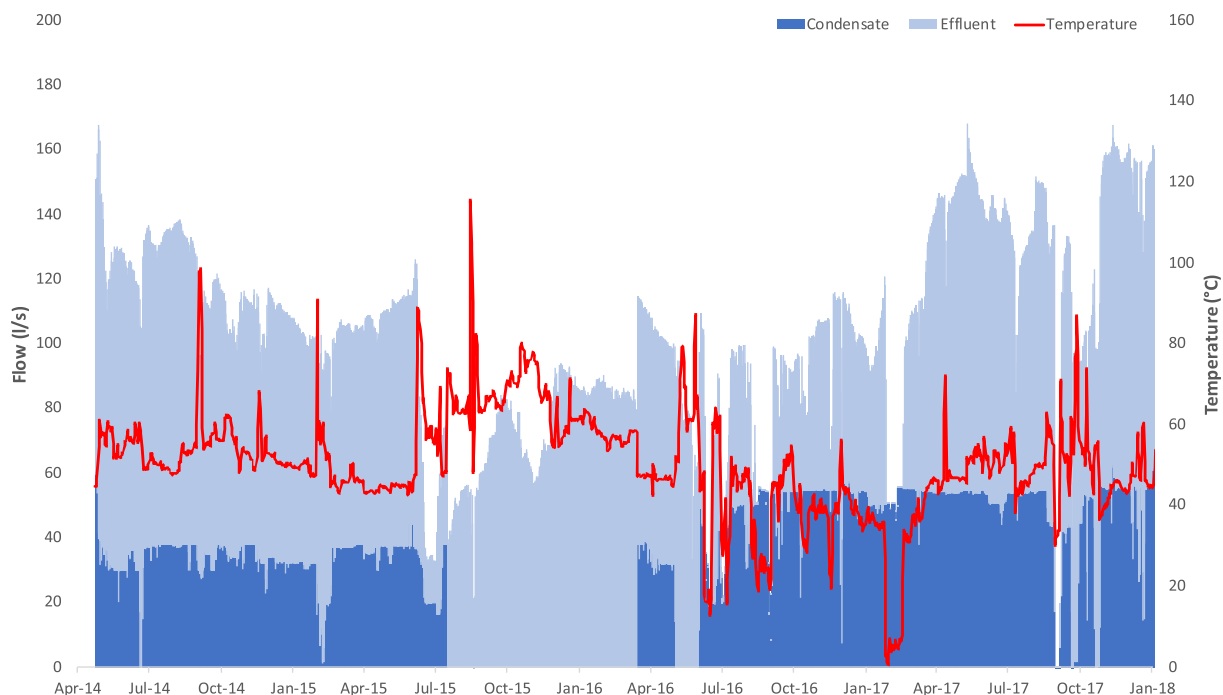
Fig. 2. Temporal evolution of the effluent water flow (light blue area) and condensate water flow (dark blue area), and the calculated temperature of the combined fluids (red line) in the HN-16 injection well. Note that condensate flow began on 22 April 2014, while the gas capture plant was in operation from 23 June 2014. The injected condensate water was gas charged after this date. Note that the gas-charged condensate water was injected into HN-14 from 15 July 2015 to 15 March 2016, therefore this gas-charged condensate water does not appear in this figure. Modified from Sigfússon et al. (2018). (For interpretation of the references to colour in this figure legend, the reader is referred to the web version of this article.)

1482 m, respectively, from HN-16, and are directionally drilled down to depths of 2703 m, 2248 m, and 2606 m (Gunnarsson et al., 2018; Snæbjörnsdóttir et al., 2018b).

Since the start of the gas-charged condensate water injection on 23 June 2014 through the end of 2017, 23,200 metric tons of CO_2 and 11,800 metric tons of H_2S had been injected. Based on average flow rates of the effluent and gas-charged fluids reported by Sigfússon et al. (2018), Clark et al. (2018) modelled the geochemistry of the fluid exiting the injection well, which consisted of 70% geothermal effluent water at 80 °C and 30% gas-charged condensate water at 20 °C. The calculated temperatures of the combined mixed injection fluids throughout the study period are shown in Fig. 2. During the first phase of gas injection, the mixed injected fluid had an average pH of 5.4, DIC of 30.9 mM, and DS of 22.3 mM; after the gas injection rate was doubled in July 2016, the pH of the mixed fluid decreased to 4.7, but the DIC increased to 50.6 mM and DS to 31.3 mM. Geochemical calculations also indicated that most common basaltic primary and secondary minerals are undersaturated in the mixed injected fluid at the well outlet, although sulfides are supersaturated and siderite close to saturation after the mixed injection fluid is heated to 260 °C. As the heated acidic mixed injected fluid reacts with the host basalts, carbonates, sulfides, and other secondary minerals likely precipitate as these fluids move away from the injection point. The likely dissolution of the host rock minerals close to the injection wells suggests a minimal risk of pore clogging close to the wells. During the second

phase of gas injection, when CO_2 and H_2S injection rates were doubled, the saturation indices of the injected mixed fluids with respect to most primary and secondary minerals are further lowered in the fluids within and adjacent to the injection well (Clark et al., 2018).

Comprehensive tracer tests were conducted during 2013–2015 to constrain the fluid pathways between the injection and production wells in the Hellisheiði geothermal field, including HE-31, HE-48, and HE-44, and the HN-17 injection well. Note HN-17 is next to and has the same trajectory as HN-16 (see Fig. 1). All three monitoring wells lie on a major fault zone on the western flanks of the Hengill volcanic system with HE-44 having the highest enthalpy of the three. Using these tracer test results, Tómasdóttir (2018) developed a simplified TOUGH2 model of the system to model the flow channels between the HN-17 injection well and the three monitoring wells using a multichannel approach. This model set the permeability to 1×10^{-12} m^2 and assigned porosity values of 0.2–3.5% to different flow channels. The study concluded that flow paths are lengthened by the sinking of cool injected fluids, thus increasing water-rock interaction and reducing the potential cooling effect of the injected fluids on the fluids collected from the monitoring wells.

Once in the geothermal reservoir, heat exchange and host rock dissolution saturates the gas-charged fluid with respect to various carbonate and sulfur minerals. The mass of carbonate and sulfate minerals precipitated from these waters was quantified using an inert chemical tracer.

In total, 405 kg of a thermally stable inert tracer, 1-naftalenesulfonic acid (1-ns), was mixed into the injected gas-charged condensate water stream to monitor the sub-surface transport, dilution, and mixing, and to assess the degree of subsurface carbonation and sulfide precipitation from 23 June 2014 to 15 March 2016. The first arrival of the tracer from the HN-16 injection well to the HE-31, HE-48, and HE-48 was observed after 15, 30, and 94 days, respectively, after the injection of the tracer. Note that the flow path from injection well HN-16 is north/northeast towards the three monitoring wells, while the flow path of injection well HN-14 deviates more towards the northwest. Consequently, the gas mixture and tracer injected into HN-14 from 15 July 2015 to 15 March 2016 flowed outside the CarbFix2 site and was not observed in the monitoring wells.

Gunnarsson et al. (2018) reported that the permeability of the target CarbFix2 injection reservoir remained stable throughout the first year and a half of the injection. This observation was attributed to (1) the acidic injected gas-charged fluids tendency to dissolve material close to the injection well but only precipitate minerals away from the injection well, and (2) the relatively small amount of mineral precipitates compared to the size of the reservoir; it is estimated that calcite and pyrite filled no more than 0.001 vol percent of the pore space in the target aquifer during the first 1.5 years of the injection.

3. METHODS

3.1. Sampling and analysis

A total of 76 samples were collected from the three monitoring wells at the Hellisheiði geothermal power plant (Fig. 1). The steam and water phases of the samples were collected using a Webre separator. The pH of the water phase was measured on site with an estimated uncertainty of ±0.1 using a flow cell connected to a cooling spiral to prevent degassing of CO_2 and H_2S and influx of O_2. All water samples were filtered on site through 0.2 μm Millipore cellulose acetate filters using a 142 mm Sartorius filter holder. Samples for 1-ns tracer measurements were filtered into 60 mL amber glass bottles and analyzed using a Thermo Ultimate 3000 High Pressure Liquid Chromatography with a BetaBasic C-18 column and fluorimetric detection. The detection limit for 1-ns is 5×10^{-7} mM (Gunnarsson et al., 2018).

Major dissolved elements and anions, other than carbon- and sulfide-derived anions, of the water samples were measured using a Dionex ICS-2000 Ion Chromatography (IC), a Spectro Ciros Vision Inductively Coupled Plasma Optical Emission Spectrometer (ICP-OES), and a Thermo Scientific iCAPQc Inductively Coupled Plasma Mass Spectrometer (ICP-MS). Water subsamples to be analyzed by ICP-OES and ICP-MS were acidified on site with concentrated supra-pure HNO_3 (1.0 vol%) while no preparation was required for IC analysis of Cl^- and F^-. For the determination of sulfate (SO_4^{-2}), water subsamples were treated on site with zinc acetate to precipitate sulfide (S^{2-}) as zinc sulfide preventing H_2S oxidation to SO_4 upon storage. These subsamples were then filtered again through 0.2 μm cellulose acetate filters before analysis by IC. Water samples for DIC determination were filtered and collected in 300 mL amber glass bottles and analyzed by alkalinity titration, while a 0.5 mL water sample taken for H_2S analysis was titrated on site using 0.001 M mercuric acetate; both analysis methods are described in detail by Arnorsson et al. (2006). Analytical uncertainties of these analyses were on the order of ≤5% and the detection limits listed in the Supplementary Material.

Steam samples were collected into 250 mL pre-evacuated gas bulbs containing 5–10 mL of a 50% aqueous KOH solution. The composition of these samples were measured using an Agilent Technologies 7890 A gas chromatography system using a HP-Molesieve (19095P-MSO) column and Thermal Conductivity Detector for H_2, O_2, N_2, and CH_4. The H_2S in the steam phase, after its dissolution into the KOH rich aqueous solution, was analyzed by titration with silver nitrate and silver electrode endpoint detection (Metrohm 905 Titrando), while the CO_2 in the steam samples was analyzed by alkalinity titration following the method of Arnorsson et al. (2006). Analytical uncertainties of these analyses were on the order of ≤5%.

3.2. Geochemical calculations

The WATCH speciation program (Arnorsson et al., 1982; Bjarnason and Arnorsson, 2010) was used to calculate the major element concentrations of the original geothermal reservoir fluids before its phase separation during sampling. As the three monitoring wells are liquid enthalpy wells (Gunnarsson et al., 2018), the steam fraction at the sample collection pressure was determined assuming adiabatic boiling from the reservoir temperature to the sampling pressure (Arnorsson et al., 2007). Since the total concentration of hydrogen was not measured, the pH was calculated by the WATCH program using charge balance constraints and the concentration of some components in the original geothermal fluid (Bjarnason and Arnorsson, 2010).

Studies of Icelandic geothermal fields concluded that local chemical equilibrium is closely approached between the fluids and hydrothermal minerals at temperatures as low as 50 °C for all major components, except Cl. Thus geothermal fluid temperatures can be estimated with the help of geothermometers based on certain elements (Arnórsson et al., 2008). Based on the previously measured downhole temperatures and characterization of the Hellisheiði geothermal reservoir (Franzson et al., 2010, 2005; Gunnarsson et al., 2018), the reservoir temperature was calculated assuming the fluid phase was in equilibrium with quartz (Gunnarsson and Arnorsson, 2000) using a silica geothermometer equation derived from the experimentally determined solubility of quartz in water for temperatures (°C) up to 330 °C:

$$T^\circ_{quartz}C = -42.198 + 0.28831 \times [Si] - 3.6686 \cdot 10^{-4}$$
$$\times [Si]^2 + 3.1665 \cdot 10^{-7} \times [Si]^3 + 77.034 \times \log[Si]$$

$$(1)$$

where [*Si*] represents the silica concentration in mg/kg (Fournier and Potter, 1982). Temperatures estimated in this manner are referred to as 'quartz temperatures' below and are estimated to have an uncertainty <2%.

The geochemical speciation program PHREEQC 3.4.0 (Parkhurst and Appelo, 2013) was then used together with the *carbfix* database (Voigt et al., 2018a), which itself was modified from the *core10* database (Neveu et al., 2017) to determine the saturation index of the sampled fluids with respect to relevant primary and secondary minerals (Clark et al., 2018; Snæbjörnsdóttir et al., 2018b) (Table S-1). The saturation index is defined as $SI \equiv \log_{10}\Omega$; the saturation state, Ω, is calculated from $\Omega \equiv Q/K_{SP}$, where K_{SP} represents the equilibrium constant of the mineral dissolution reaction, and Q denotes the corresponding reaction quotient of the combined fluid sample. A sample is supersaturated with a mineral if its saturation index is greater than zero and undersaturated if it is less than zero.

To create mineral predominance diagrams, the computer program PhreePlot (Kinniburgh and Cooper, 2011), which is embedded with PHREEQC, was used together with the *carbfix* database and the average fluid concentrations and temperatures sampled from the monitoring wells. Pourbaix diagrams were generated using the Geochemist's Workbench Version 12, the *LNLL thermo* database, and the average sampled fluid concentrations and temperatures. As wells HE-31 and HE-48 had similar compositions and the same average reservoir temperature, these monitoring wells were grouped together in the mineral predominance and Pourbaix diagrams and a separate set of diagrams created for HE-44.

3.3. Mass balance and mineralization calculations

The concentrations of the major elements, if no mineral-fluid reactions occurred after the injection of fluids ($C_{i,predicted}$), were determined assuming the non-reactive mixing of the injected and formation waters. The mixing ratio of these fluids was determined from the measured concentrations of the injected non-reactive tracers in the sampled monitoring well fluids (C_{1-ns}). Taking account of mass balance constraints, $C_{i,predicted}$ was determined from Matter et al. (2016) (see the Supplementary Material for the derivation of this equation):

$$C_{i,predicted} = \frac{C_{i,background} \cdot (C_{1-ns,injected} - C_{1-ns}) + A \cdot C_{1-ns,injected} \cdot (C_{1-ns} - C_{1-ns,background})}{(C_{1-ns,injected} - C_{1-ns,background})} \tag{2}$$

where C_i designates the concentration of the component *i*, and *A* the molar ratio between the element and the tracer, 1-ns, in the mixed injection water (Table S-2); these were calculated using the average mixed injection fluid compositions and well flow rates of the gas-charged condensate and effluent waters (Clark et al., 2018; Sigfússon et al., 2018).

The background concentration of the *i*th element in the reservoir fluids ($C_{i,background}$), were calculated by averaging the concentrations of this element in the monitoring wells samples collected before the arrival of the gas-charged injection water (the samples averaged are italicized in Tables S-3 to S-5 in the Supplementary Material). As 1-ns had been used in the previous tracer tests, a dilute background concentration of 1-ns was present in the reservoir fluid ($C_{1-ns,background}$). This background concentration in wells HE-31, HE-48, and HE-44 was determined to be 6.95×10^{-7} mM. The average amount of 1-ns tracer injected ($C_{1-ns,injected}$) into HN-16 was 1.15×10^{-3} mM in the gas-charged condensate water and 3.35×10^{-4} mM in the fluid mixture (gas-charged condensate + effluent water).

Since no further tracer was injected into HN-16 after 15 July 2015, to quantify the effects of doubling the gas injection, the tracer recovery results at the monitoring wells of the 2014–2015 tracer test were extrapolated and applied from 15 July 2016. This extrapolation was performed by first fitting a third degree polynomial curve to each monitoring well's tracer concentrations over time starting from when the tracer first appeared (Figs. S-2 to S-4). Thus by knowing the start date of the original tracer injection, 23 June 2014, it was assumed that the same proportion of tracer was injected with the gas-charged water from 15 July 2016. For each monitoring well, tracer concentrations relative to the sampling dates after July 2016 were determined using the respective polynomial curves, and added to the measured tracer remaining from the first phase; this total is C_{1-ns} in Eq. (2). This approach requires the assumption that the flow channels between HN-16 and the monitoring wells remained identical throughout this study's monitoring period, which is consistent with the near constant permeability observed in the system.

Comparison of the measured (C_i) and calculated non-reactive DIC and DS concentrations in the monitoring wells allows for the calculation of the fraction of gases mineralized in the subsurface, using the following equation from Gunnarsson et al. (2018):

$$Fraction\ Mineralized = \frac{(C_{i,predicted} - C_i)}{(C_{i,predicted} - C_{i,background})} \tag{3}$$

4. RESULTS

The composition of all collected liquid and steam samples are presented in Tables S-3 to S-5 in the Supplementary Material. The recalculated compositions before phase separation are shown in Figs. 3–5.
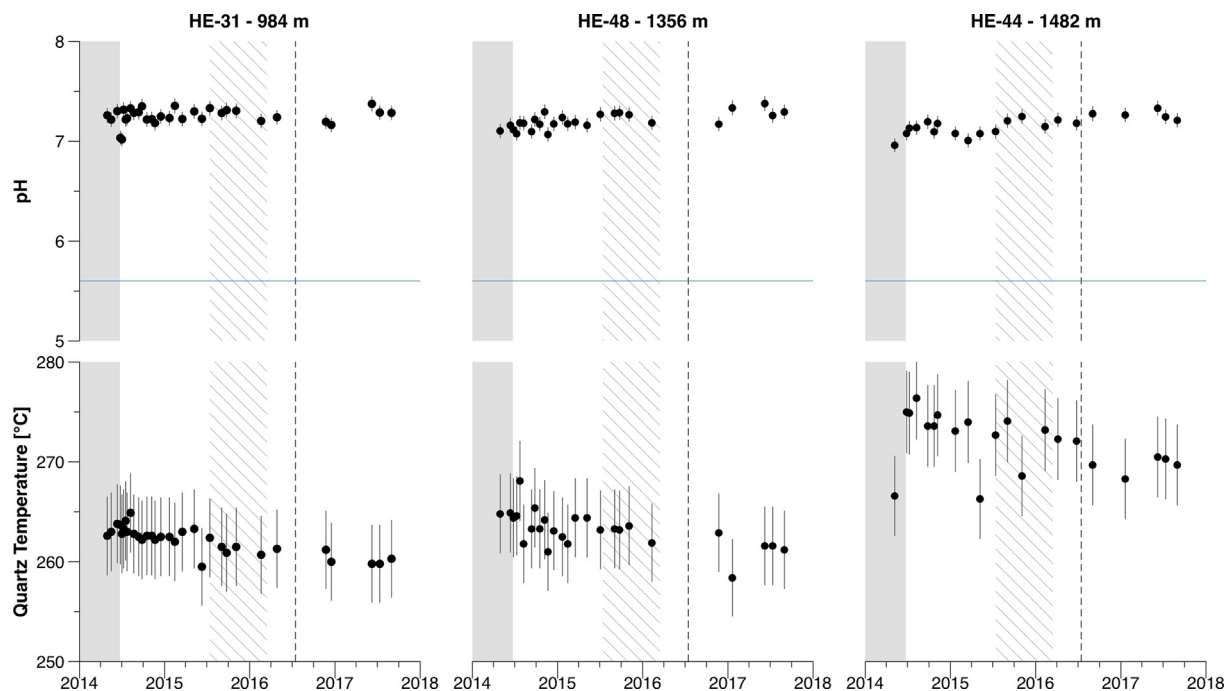
Fig. 3. The in situ pH and the reservoir temperature based on the quartz geothermometer in the HE-31, HE-48, and HE-44 monitoring wells located 984, 1356, and 1482 m, respectively, from the HN-16 injection well prior to and during the injection of CO_2 and H_2S charged waters. The symbols illustrate the measured fluid values, the gray shaded area indicates the time before the injection of gas-charged waters into well HN-16, the diagonal lines denote times when well HN-14 was used for the injection of gas-charged waters, and the vertical dashed line signifies the time when the amount of CO_2 and H_2S injected was doubled. Note that the horizontal blue line plotted in the top diagrams represents the neutral pH of 5.6 at 250 °C.

4.1. Major element concentrations in the sampled monitoring well fluids

Sampling of the liquid and steam phases at the three monitoring wells for this study began on 29 April 2014, prior to the gas-charged water injection starting on 23 June 2014. The pre-gas injection samples are highlighted in gray in Figs. 3–9. Injection of gas-charged water occurred mainly into well HN-16, except from 14 July 2015 to 15 March 2016 (a time period signified by diagonal lines in these figures), and the rate of dissolved gas injected into HN-16 was doubled on 15 July 2016, as denoted on these figures by vertical dashed lines. The gas-charged water injected into HN-14 was not observed in the monitoring wells.

The quartz temperature is reported in Fig. 3 along with the calculated *in situ* pH for all three wells. The pH exhibits no significant change throughout the injection, whereas the reservoir temperature shows a small decrease post-injection and compares well to previous downhole temperature measurements, for example with the temperature logs of HE-31 in Fig. S-1 in the Supplementary Material.

Figs. 4 and 5 compare the *in situ* major element concentrations as well as DIC and DS to those calculated assuming non-reactive fluid mixing using Eq. (2). Of the three major divalent cations, Ca had the highest concentrations with Fe and Mg concentrations close to or at the detection limit (Fig. 4). Ca and Mg show a brief peak in concentration in monitoring well HE-31 upon the first arrival of the gas-charged injection water. There was a decrease in the fluid phase Ca concentrations observed in both HE-31 and HE-48 concurrent with a gradual increase in observed DIC and an even more gradual increase in DS over time. Results from HE-44 show minimal changes in DS but a decrease in DIC post injection.

As seen in Fig. 5, both fluid Na and K concentrations increased until 2015, particularly in HE-31 and HE-48, but then these elements decreased, only increasing again when the gas injection was switched into well HN-14 and back again to HN-16. Aluminium concentrations show a similar pattern as Ca in that there was a brief peak in concentration in well HE-31 before gradually decreasing. The decline was less apparent in wells HE-48 and HE-44; these wells are further from the injection well than HE-31. The concentration of the anions, Cl, F, and B, all changed in concentration over time, though to a much lesser extent compared to Ca and Al. The least variance between concentrations calculated from non-reactive mixing and observed concentrations was in well HE-44.

4.2. Saturation indices of primary and secondary minerals

Saturation indices (SI) of the collected monitoring well fluids with respect to the primary minerals present in the basalt and of basaltic glass are shown in Fig. 6. Leached basaltic glass ($SiAl_{0.35}O_2(OH)_{1.05}$) was always undersaturated in the monitoring well fluids, and the doubling of the gas injection rate in 2016 had little effect on this
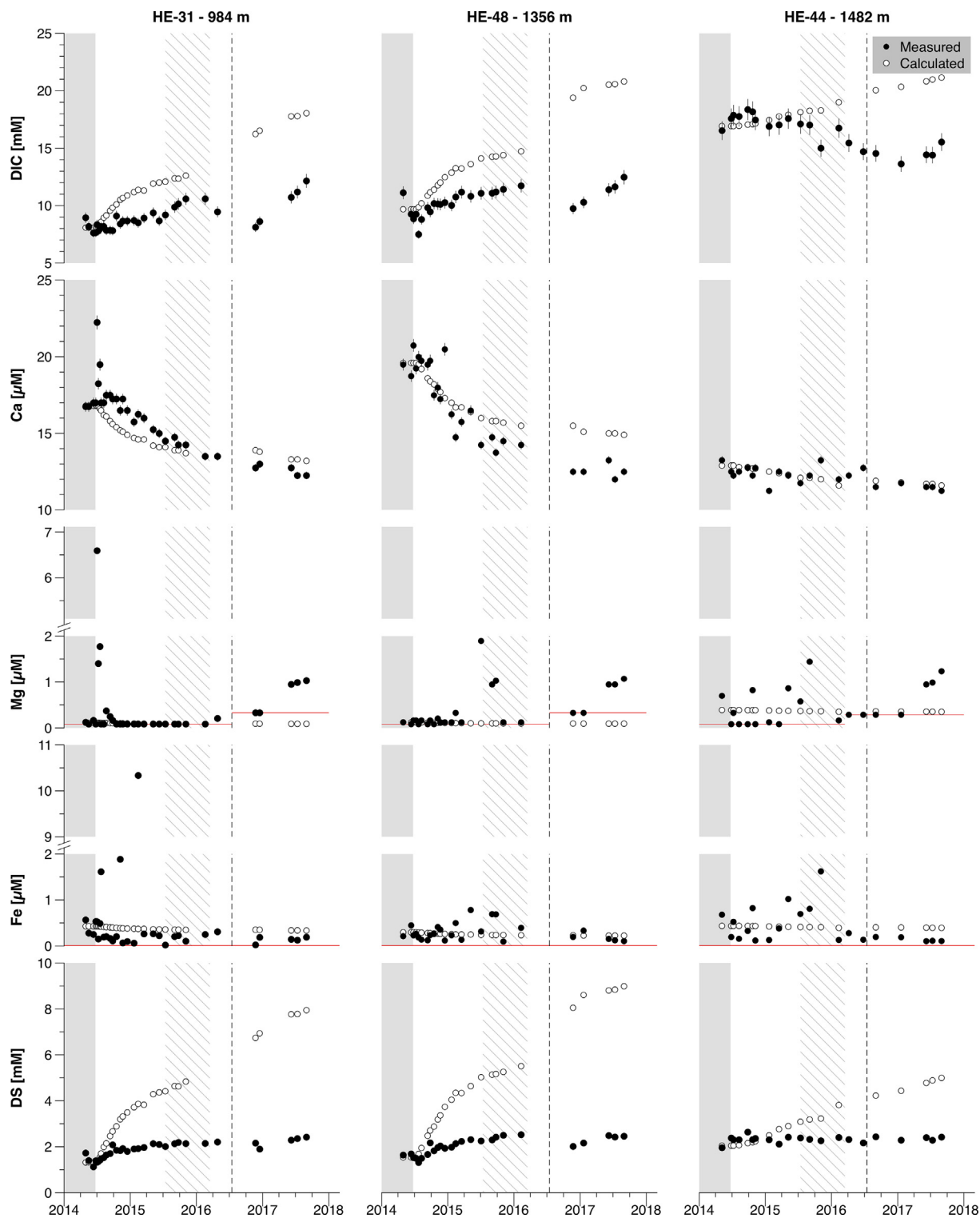
Fig. 4. In situ concentrations of DIC, Ca, Mg, Fe, and DS in samples collected from the HE-31, HE-48, and HE-44 monitoring wells located 984, 1356, and 1482 m, respectively, from the HN-16 injection well prior to and during the injection of CO_2 and H_2S. The gray shaded area indicates the time before the injection of gas-charged waters into well HN-16, the diagonal lines denote the times when well HN-14 was used for the injection of gas-charged waters, and the dashed line signifies the time when the amount of CO_2 and H_2S injected was doubled. Black circles depict the measured concentrations, while the white circles correspond to concentrations calculated assuming non-reactive fluid mixing using Eq. (2). The red lines are the limit of detection for Mg and Fe concentrations.
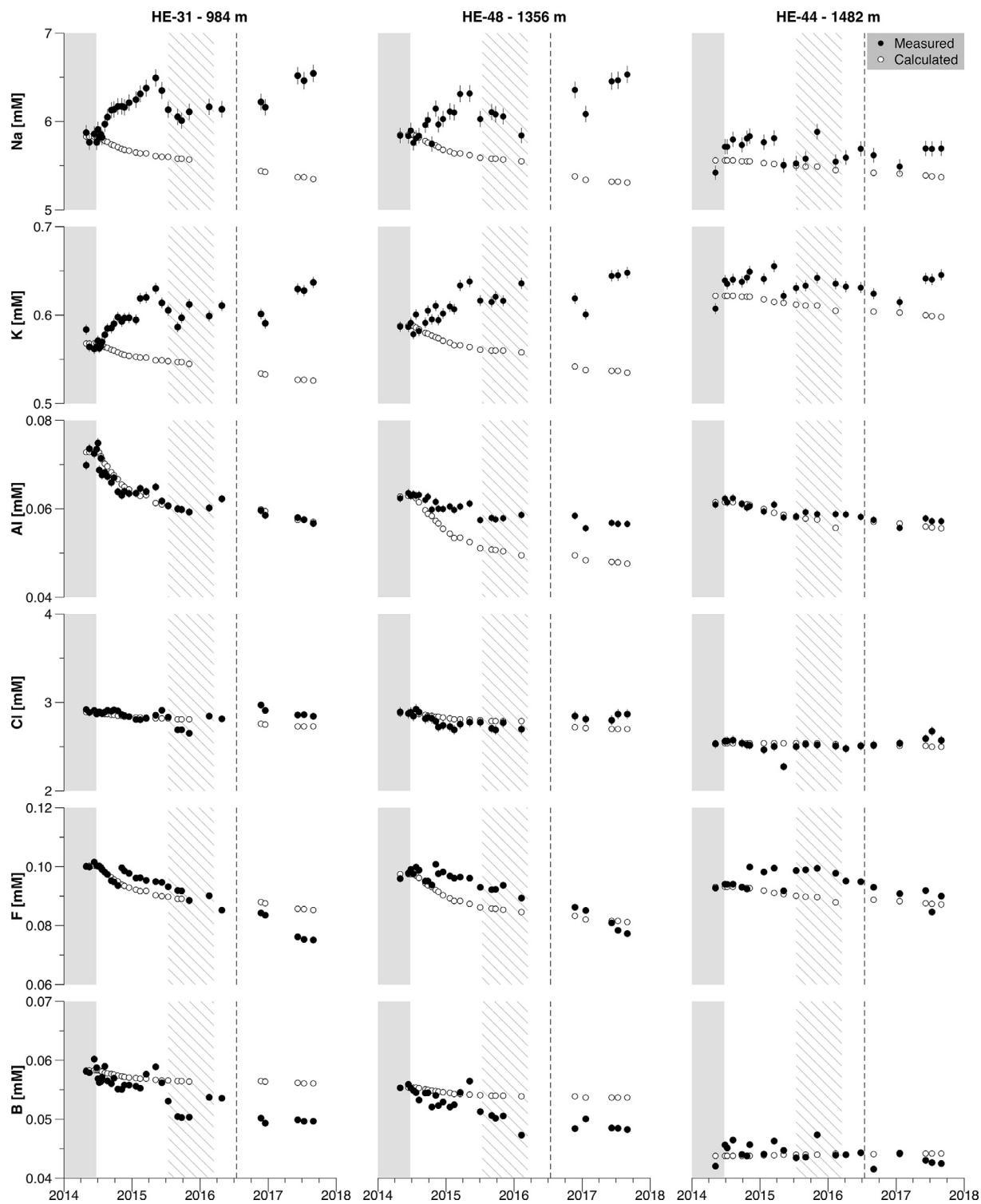
Fig. 5. In situ concentrations of Na, K, Al, Cl, F, and B in samples collected from the HE-31, HE-48, and HE-44 monitoring wells located 984, 1356, and 1482 m, respectively, from the HN-16 injection well prior to and during the injection of CO_2 and H_2S. The gray shaded area indicates times before injection of gas-charged water into well HN-16, the diagonal lines denote when well HN-14 was used for the injection of gas-charged water, and the dashed line signifies the time when the amount of CO_2 and H_2S injected was doubled. Black circles depict the measured concentrations, while the white circles correspond to concentrations calculated assuming non-reactive fluid mixing using Eq. (2).
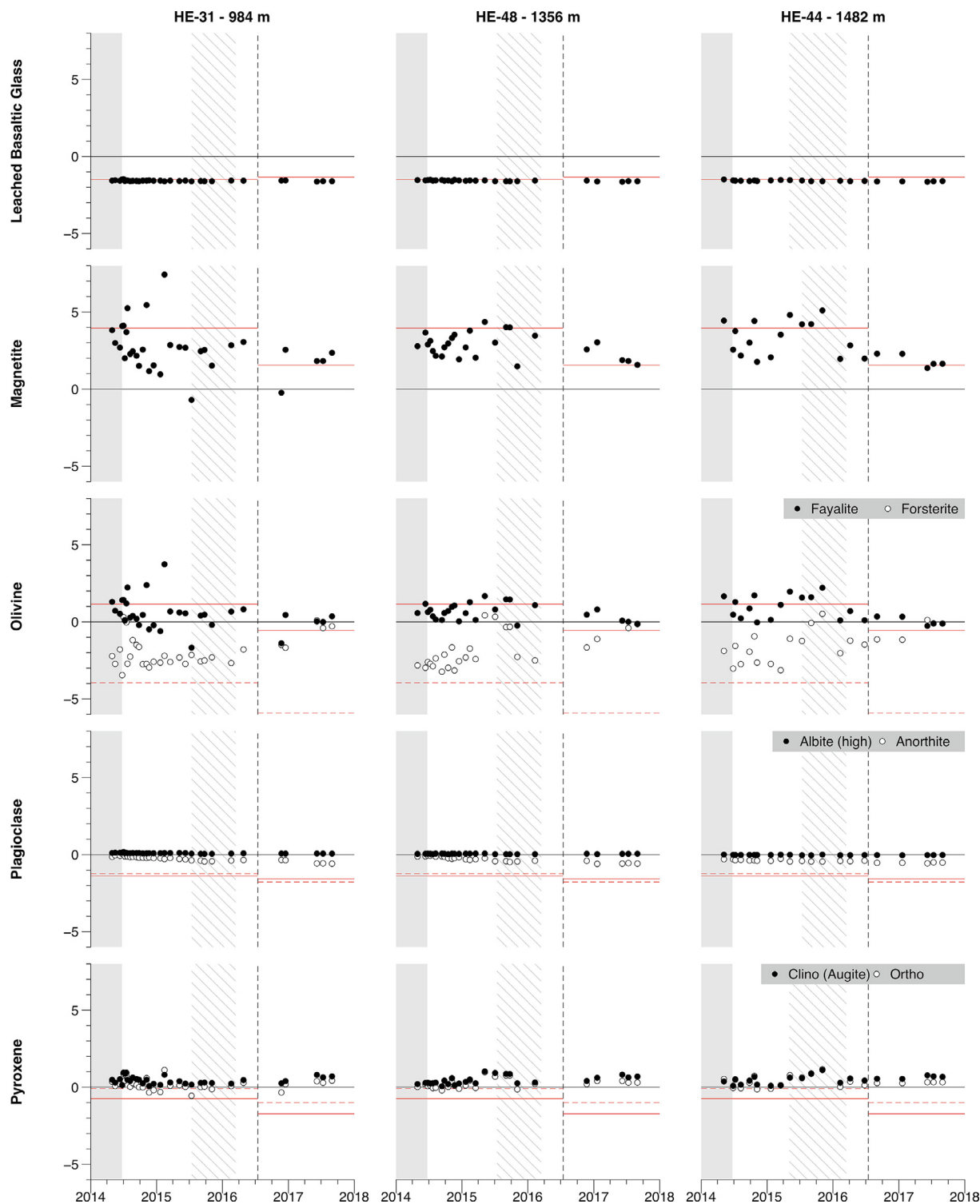
Fig. 6. The in situ saturation indices (SI) of the fluids collected from the HE-31, HE-48, and HE-44 monitoring wells with respect to the primary minerals found in unaltered basalt at Hellisheiði – magnetite, olivine, plagioclase, and pyroxene, and leached basalt glass. The black and white symbols correspond to the saturation index of the collected fluids, the gray shaded area indicates the time prior to the injection of gas-charged waters into well HN-16, the diagonal lines denote when well HN-14 was used for the gas-charged water injection, and the vertical dashed line signifies the time when the amount of CO_2 and H_2S injected was doubled. The SI of the minerals in the injected gas-charged consdensate water, after mixing with geothermal effluent water and their heating to 260 °C, but prior to their interaction with the rock (Clark et al., 2018), are depicted as horizontal and dotted red lines. The minerals in black circles are represented by the horizontal red line and the minerals in white circles by the dotted red line.
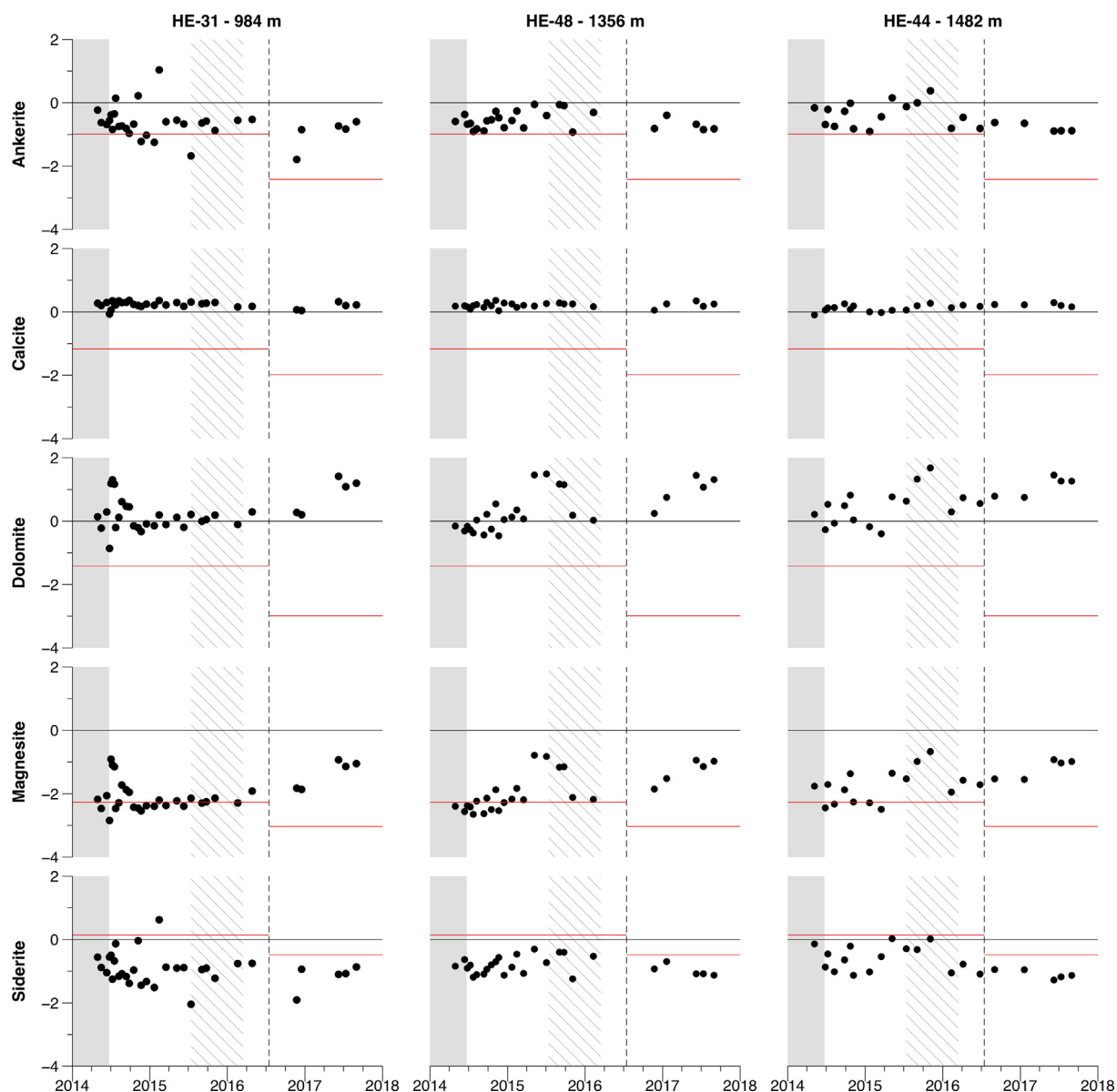
Fig. 7. In situ saturation indices (SI) of the fluids collected from the HE-31, HE-48, and HE-44 monitoring wells with respect to the carbonate minerals – ankerite, calcite, dolomite, magnesite, and siderite. The black symbols corespond to calculated fluid saturation indexes, the gray shaded area indicates times before the injection of gas-charged water into well HN-16, the diagonal lines denote times when well HN-14 was used for the injection of gas-charged waters, and the vertical dashed line signifies the time when the amount of CO_2 and H_2S injected into the subsurface was doubled. The SI of these mineral in the injected gas-charged waters, after mixing with geothermal effluent water and heating to 260 °C, but prior to their interaction with the rock (Clark et al., 2018), are depicted by horizontal red lines.

saturation index. Magnetite, however, was supersaturated throughout the monitoring period. The plagioclase endmembers were close to saturation in the collected monitoring well fluids over the entire study period with high-albite right at saturation and anorthite just below. The heated mixed injection water was undersaturated with respect to both of these plagioclase endmembers. The saturation index of the monitoring well fluids with respect to clinopyroxene (augite) and orthopyroxene were mostly at saturation or supersaturated in contrast to their undersaturated state in the heated mixed injected fluids. The saturation index of

the olivine endmembers show the largest changes between the heated mixed injection and monitoring well fluids, as well as the greatest variation, though fayalite was supersaturated in the monitoring well fluids during the first two years of injection.

Fig. 7 shows the saturation indices of the collected monitoring well fluids with respect to various carbonate minerals – ankerite ($CaFe(CO_3)_2$), calcite ($CaCO_3$), dolomite ($CaMg(CO_3)_2$), magnesite ($MgCO_3$), and siderite ($FeCO_3$) – compared to that of the heated mixed injected gas-charged fluid. Calcite was consistently at saturation or
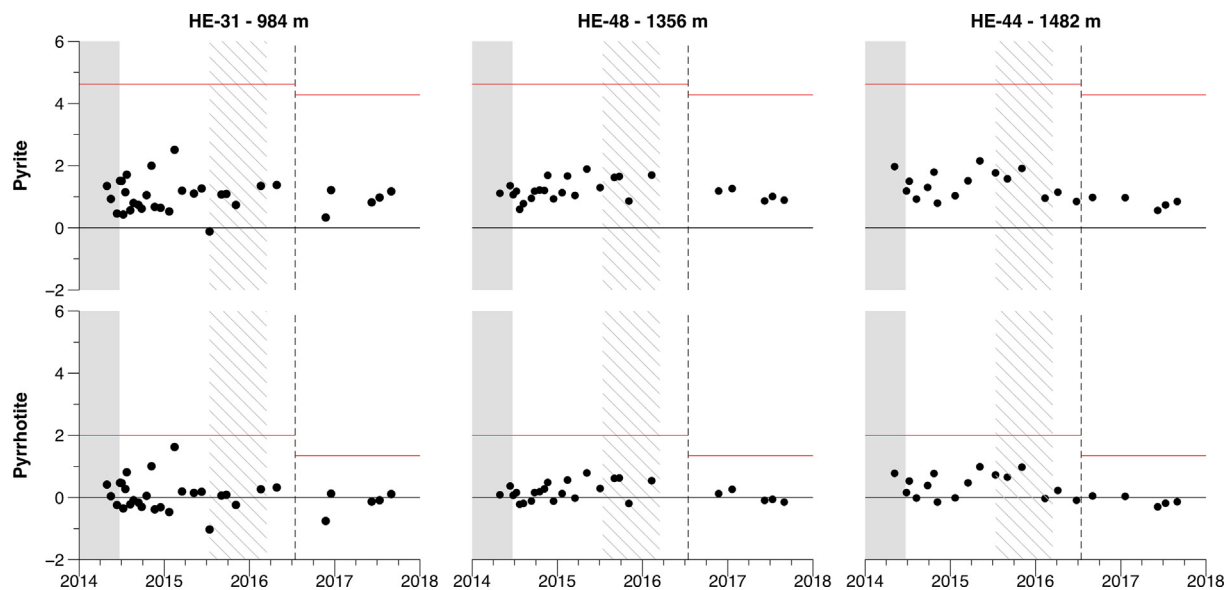
Fig. 8. In situ saturation indices of the fluids collected from monitoring wells HE-31, HE-48, and HE-44 with respect to the sulfide minerals, pyrite and pyrrhotite. The symbols correspond to the calculated saturation index, the gray shaded area indicates time prior to the injection of gas-charged water into well HN-16, the diagonal lines denote times when when gas-charged waters were injected into well HN-14, and the vertical dashed line signifies the time when the amount of CO_2 and H_2S gas injected was doubled. The SI of these minerals in the injected gas-charged waters, after mixing with geothermal effluent water and its heating to 260 °C, but prior to their interaction with the rock (Clark et al., 2018), is depicted as horizontal red lines.

supersaturation in the monitoring well fluids. Dolomite was also at equilibrium (within uncertainty) in these fluids and then supersaturated during the second phase of gas injection. Magnesite was always undersaturated, whereas siderite and ankerite were undersaturated in these fluids with few exceptions.

The saturation indices of these fluids with respect to the iron sulfide phases, pyrite (FeS_2) and pyrrhotite (FeS), are presented in Fig. 8. Both minerals were supersaturated in the heated mixed injection and monitoring wells fluids. They were, however, closer to saturation in the latter.

The saturation indices of the subsurface fluids with respect to some of the secondary minerals commonly observed in high temperature Hellisheiði basalts are presented in Fig. 9. These minerals include chlorite ((Mg/Fe)$_5$-Al$_2$Si$_3$O$_{10}$(OH)$_8$), epidote (Ca$_2$FeAl$_2$Si$_3$O$_{12}$(OH)), prehnite (Ca$_2$Al$_2$Si$_3$O$_{10}$(OH)$_2$), wairakite (CaAl$_2$Si$_4$O$_{10}$(OH)$_4$), wollastonite (CaSiO$_3$), and actinolite (Ca$_2$(Fe/Mg)$_5$Si$_8$O$_{22}$(-OH)$_2$). Many of these minerals were found to be stable throughout the mixed gas injection, with epidote and prehnite supersaturated, wairakite at saturation, and wollastonite just undersaturated. The saturation indices of the fluids with respect to actinolite and chlorite fluctuated with both actinolite endmembers above saturation and the Fe-chlorite endmember (daphnite) more stable. Mg-chlorite (clinochlore) became supersaturated in the subsurface fluids after doubling the gas injection.

4.3. Partial pressure of CO_2 and H_2S

The temporal evolution of the *in situ* partial pressure of CO_2 and H_2S (pCO_2 and pH_2S) of the fluids collected from the monitoring wells is shown in Fig. 10, with red lines denoting the average pCO_2 and pH_2S in the heated mixed gas-charged injection fluids before dilution and water-rock interaction in the reservoir. Both pCO_2 and pH_2S increased upon the arrival of the gas-charged injection fluids to the first two monitoring wells. There was a noticeable drop, particularly in pCO_2, after well HN-14 was used for gas injection, before rising again after the amount of gas injected was doubled and again injected into HN-16. Results from HE-44 show minimal change in pH_2S and a small decrease in pCO_2, which was similar to the observed DIC and DS concentrations (Fig. 4).

5. DISCUSSION

The pCO_2 and pH_2S in equilibrium with the minerals relevant for carbon and sulfur storage are plotted together with the composition of collected monitoring well samples in Fig. 11. Fig. 11A confirms that the monitoring well temperatures are close to the upper stability limit of calcite at the current DIC levels. This is further supported by the mineral saturation indices of the collected fluids. Fig. 11B shows that the compositions of the collected monitoring well fluids are also close to the decomposition temperature of iron sulfide minerals. As pointed out by Stefánsson et al. (2011), the precipitation of pyrite and pyrrhotite is slowed by epidote formation at temperatures above ~260 °C, consequently requiring a larger amount of basalt dissolution for H_2S mineralization. The Eh-pH diagrams of the H_2S-H_2O-Fe system (Fig. 12) indicate that redox conditions in the monitoring well fluids are close to or at equilibrium with pyrite and magnetite.
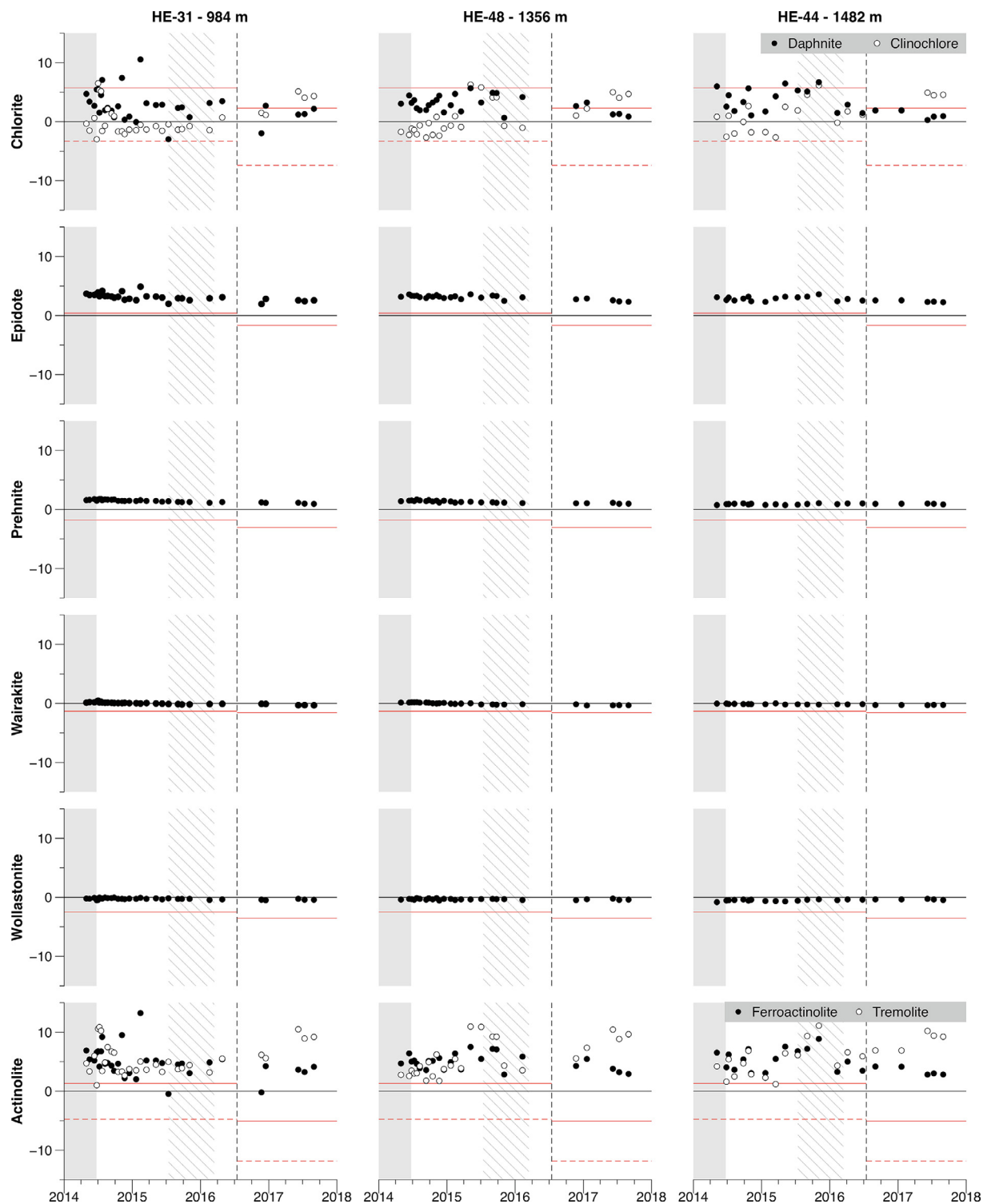
Fig. 9. In situ saturation indices (SI) of the fluids collected from the HE-31, HE-48, and HE-44 monitoring wells with respect to the secondary minerals observed in the higher temperature regions of the Hellisheiði geothermal reservoir (Snæbjörnsdóttir et al., 2018b). The gray shaded area indicates times before gas-charged water injection into well HN-16, the diagonal lines denote times when the HN-14 well was used for injection, and the vertical dashed line signifies the time when the amount of CO_2 and H_2S injected was doubled. The SI of minerals in the injected gas-charged waters, after mixing with geothermal effluent water and heated to 260 °C, but prior to their interaction with the rock (Clark et al., 2018), are depicted as horizontal and dotted red lines. The minerals in black circles are represented by the horizontal red line and the minerals in white circles by the dotted red line.
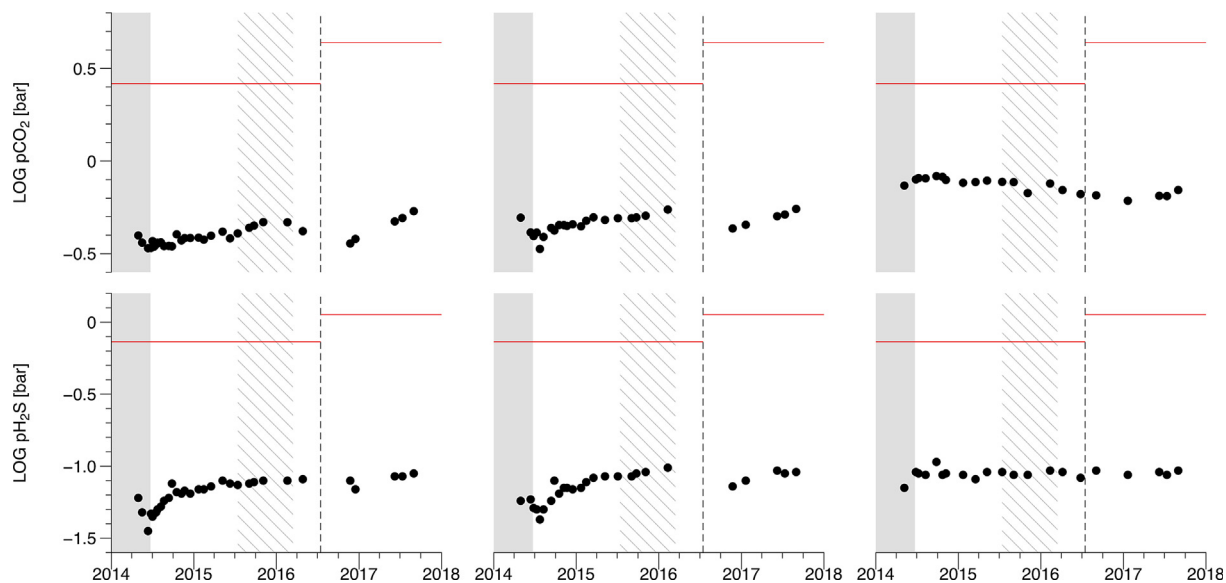
Fig. 10. Logarithm of the in situ pCO$_2$ and pH$_2$S of the fluids collected from the HE-31, HE-48, and HE-44 monitoring wells. The gray shaded area indicates the time prior to the injection of gas-charged waters into well HN-16, the diagonal lines denote times when well HN-14 was used for the gas-charged water injection, and the vertical dashed line signifies the time when the amount of CO$_2$ and H$_2$S injected was doubled. Horizontal red lines depict the logarithim of the pCO$_2$ and pH$_2$S of the injected gas-charged waters, after mixing with geothermal effluent water and heated to 260 °C, but prior to their interaction with the rock and mixing with formation waters.
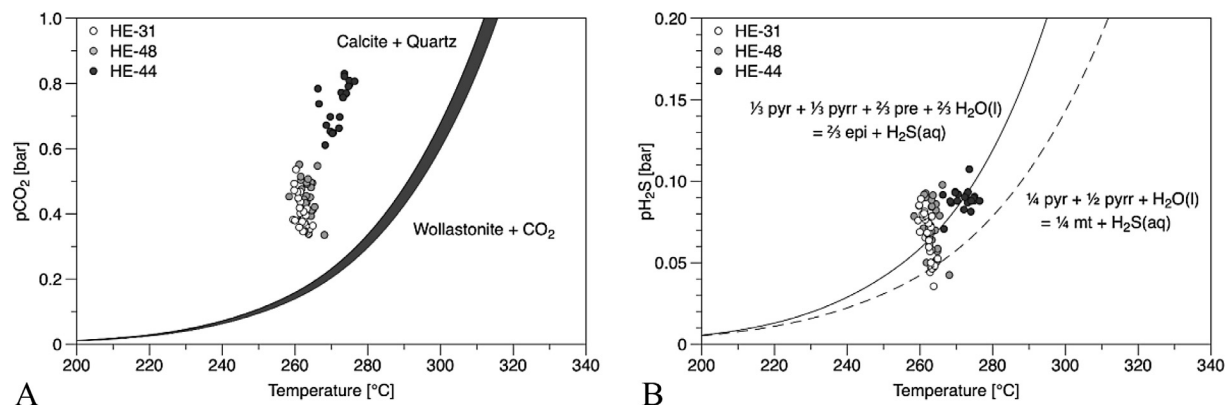

Fig. 11. The in situ pCO$_2$ and pH$_2$S of the fluids collected from the HE-31, HE-48, and HE-44 monitoring wells plotted against the calculated reservoir temperature. Curves represent the partial pressures of the indicated gases in equilibrium as a function of temperature according to the following mineral-gas reactions: (A) the formation of wollastonite and CO$_2$ from calcite and quartz at fixed total pressures from 1 to 300 bars based on Skippen (1977); (B) the formation of epidote (epi) and H$_2$S from pyrite (pyr), pyrrhotite (pyrr) and prehnite (pre), represented by the solid curve, and the formation of magnetite (mt) and H$_2$S from pyrite, pyrrhotite, and H$_2$O, represented by the dashed curve, based on data reported by Arnorsson et al. (2007) and Stefánsson et al. (2011).

Calcium was the most abundant divalent cation in the fluid phase, but its concentration continuously decreased throughout the injection as DIC rose while pH remained close to constant maintaining equilibrium with calcite. Magnesium and Fe were close to or at the detection limit, but Mg concentration increased after the injection rate was doubled (Fig. 4). This is similar to the seawater-basalt experiments of Voigt et al. (2018b) (comparable to natural marine hydrothermal vent systems) where Ca was the most abundant cation in the fluid and any available Mg and Fe had been quickly removed by their incorporation into clays. The brief peak in Ca concentration observed

when the initial gas-charged water plume arrives at the monitoring well was also observed in the pure CO$_2$ injection at the original CarbFix site (Snæbjörnsdóttir et al., 2017) and during the arrival of the CO$_2$-charged waters of the column experiment mimicking this pure CO$_2$ injection (Clark et al., 2019). In both field injections, this peak results in the formation of calcite; its precipitation continues due to the constant availability of Ca. Note that the injected fluid contains three orders of magnitude more DIC than Ca (Fig. 4), thus the Ca required for calcite precipitation must come from the rocks. Although the decrease in measured Ca concentrations are similar to the corresponding
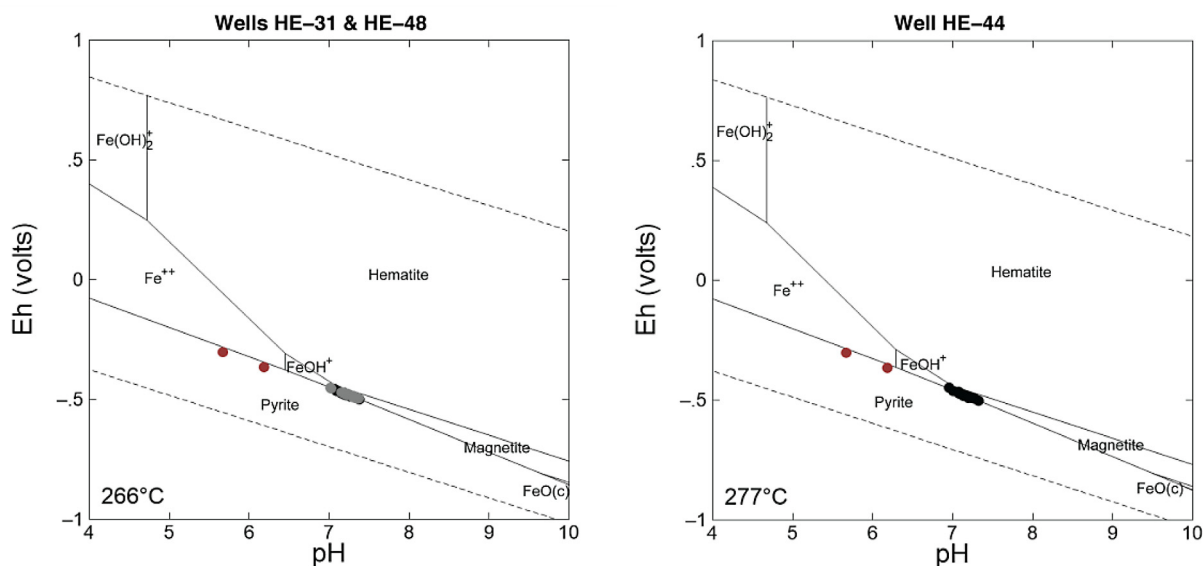
Fig. 12. Pourbaix diagrams for the H$_2$S-H$_2$O-Fe system at (A) T = 266 °C, P = 200 bars, a$_{[H2O]}$ = 1, a$_{[Fe+2]}$ = $10^{-9.98}$, a$_{[SO4-2]}$ = $10^{-4.13}$ with the in situ compositions of fluids from the HE-31 and HE-48 monitoring wells represented by black and gray points, respectively, and (B) T = 277 °C, P = 200 bars, a$_{[H2O]}$ = 1, a$_{[Fe+2]}$ = $10^{-9.93}$, a$_{[SO4-2]}$ = $10^{-4.26}$ with the deep fluid from HE-44 represented by black points. The red points represent the composition of gas injected waters mixed with geothermal brine within the well and heated to 260 °C (before any reaction or dilution in the geothermal reservoir) and the dotted lines depict the stability limits of water. The temperature, a$_{[Fe+2]}$, and a$_{[SO4-2]}$ are based on the average temperature and fluid compositions from HE-31, HE-48, and HE-44; wells HE-31 and HE-48 were grouped together because of the similar fluid compositions and same average temperature.

calculated non-reactive mixing concentrations especially during the first two years of injection, there is a steady decline in these Ca concentrations. This decline, and the fact that the dissolved Ca concentration are several orders of magnitude lower than those of DIC indicate that the release of this cation from the host rock to the fluid phase is one of the limiting factors for calcite precipitation. Several Ca-bearing secondary minerals could compete with calcite for aqueous calcium including actinolite, epidote, prehnite, and wairakite; these minerals are calculated to be saturated or supersaturated with respect to the monitoring well fluids (see Fig. 9).

Figs. 13 and 14 depict the relationship between the injection and monitoring well fluid compositions, and provide insight into the potential carbonate and other secondary minerals that form from these fluids. The mineral predominance diagrams of the carbonate system (Fig. 13) suggest that the increase in dissolved Mg concentrations and pCO$_2$ after the injection rate was doubled (see Figs. 4 and 10) favors dolomite precipitation. This suggestion is consistent with the greater supersaturation of these fluids with respect to dolomite after July 2016, as shown in Fig. 7. In contrast, thermodynamic calculations suggest that Fe will not be incorporated into siderite (Fig. 13C and D), which is consistent with its saturation indices (Fig. 7). In addition to sulfide minerals other secondary minerals, such as epidote and chlorite, likely consume the available Fe.

Basalt at the CarbFix2 site was altered before the injection by high temperature fluids forming secondary minerals from the breakdown of basaltic glass, olivine, pyroxene, and plagioclase (Franzson et al., 2010, 2005; Snæbjörnsdóttir et al., 2018b). Olivine and basaltic glass

likely alter to smectites, zeolites, chalcedony, and calcite, which was characteristic of the original CarbFix site (Alfredsson et al., 2013). As temperatures increase past about 200 °C, chalcedony is converted to quartz, smectites to mixed layer clays and eventually to chlorite. Since the reservoir temperatures around the main feed zones of the monitoring wells used in this study are greater than 250 °C, the other primary minerals in basalt, notably plagioclase, and pyroxene, are also altered. One clear sign of plagioclase alteration is the occurrence of albitization; Ca-rich plagioclase dissolves leading to albite formation (Snæbjörnsdóttir et al., 2018b), consistent with the mineral saturation indices in Fig. 6. Plagioclase was also altered to epidote and wairakite before the injection (Snæbjörnsdóttir et al., 2018b), consistent with their mineral saturation indices reported before and after the injection in Fig. 9. Additionally, the continuous net release of Na and K (Fig. 5) could be attributed to the dissolution of basaltic and altered basalt minerals like mixed layer clays and chlorites by their interaction with the acidic gas-charged injection waters. A similar mobility of Na and K was also observed in the original CarbFix site (Snæbjörnsdóttir et al., 2017).

Predominance diagrams of secondary minerals resulting from high temperature alteration, other than the carbonates and sulfides, are presented in Fig. 14. All the monitoring well samples are present in the ferroactinolite and tremolite (endmembers of actinolite) stability fields. The reaction path of the injected fluid likely passed through the Fe-chlorite (daphnite) and epidote stability fields before ending in the ferroactinolite and tremolite predominance fields during its flow from the injection well to the monitoring wells. Note that Fig. 14C and D represent the average
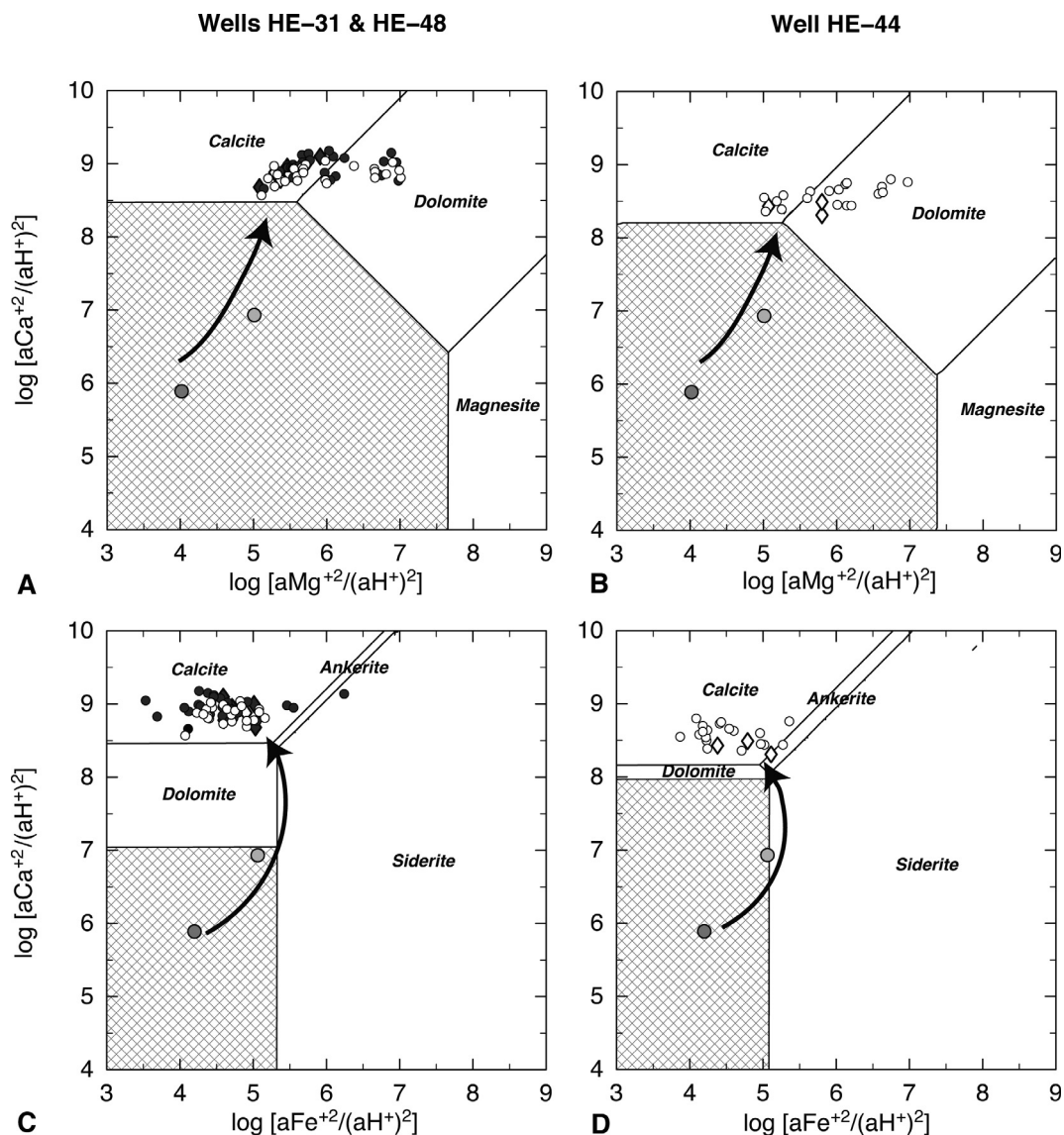
Fig. 13. Mineral predominance diagrams among carbonate minerals in the CaO-MgO-FeO-CO$_2$ system for monitoring wells (A) HE-31 and HE-48 at T = 266 °C, [Fe] = 0.482 μmol/kg, and [CO$_2$] = 9.5 mmol/kg, and (B) HE-44 at T = 273 °C, [Fe] = 0.444 μmol/kg, and [CO$_2$] = 16.5 mmol/kg, and in the CaO-MgO-FeO-CO$_2$ system for monitoring wells (C) HE-31 and HE-48 at T = 266 °C, [Mg] = 0.489 μmol/kg, and [CO$_2$] = 9.5 mmol/kg, and (D) HE-44 at T = 273 °C, [Mg] = 0.522 μmol/kg, and [CO$_2$] = 16.5 mmol/kg. The black circles represent the in situ compositions of fluids collected from HE-31 and white circles the in situ composition of fluids collected from HE-48 and HE-44 with the black and white diamonds depicting the in situ pre-injection fluid compositions for each well. The gray circles represent the gas injected waters mixed with geothermal brine within the well and heated to 260 °C (before any dilution or reaction in the geothermal reservoir) with the light gray symbols signifying the first two years of injection and the dark gray symbols these fluids after doubling the amount of gas injected. The cross-hatched area represents fluid compositions where no stable carbonate minerals are present. The temperature, [Fe], [Mg], and [CO$_2$] adopted in the figure are based on the average temperature and fluid compositions from HE-31, HE-48, and HE-44; wells HE-31 and HE-48 were grouped together because of their similar fluid compositions and same average temperature.

temperature of the fluids as they enter the monitoring wells at 266 °C (wells HE-31 and HE-48) and 277 °C (HE-44).

Although Cl⁻, F⁻, and B might be expected to exhibit a conservative behavior, these anions steadily decreased in concentration from the start of injection (Fig. 4). While Cl⁻ and B only slightly deviate from their concentrations calculated assuming non-reactive fluid mixing using Eq. (2), there was a larger variance in B accompanied by a small peak in concentrations, notably in HE-31 and HE-48. This

peak is concurrent with an increase in Na and K, suggesting the dissolution of silicate minerals. Several studies describe the potential uptake of these anions by carbonate minerals, particularly calcite. According to Kitano et al. (1975), calcite can incorporate chloride and fluoride during precipitation, while the uptake of boron has been extensively studied in Ca and Mg carbonates (e.g. Hemming et al., 1995; Saldi et al., 2018). Experiments by Turner et al. (2005) also suggest fluoride adsorption onto the surfaces of calcite in
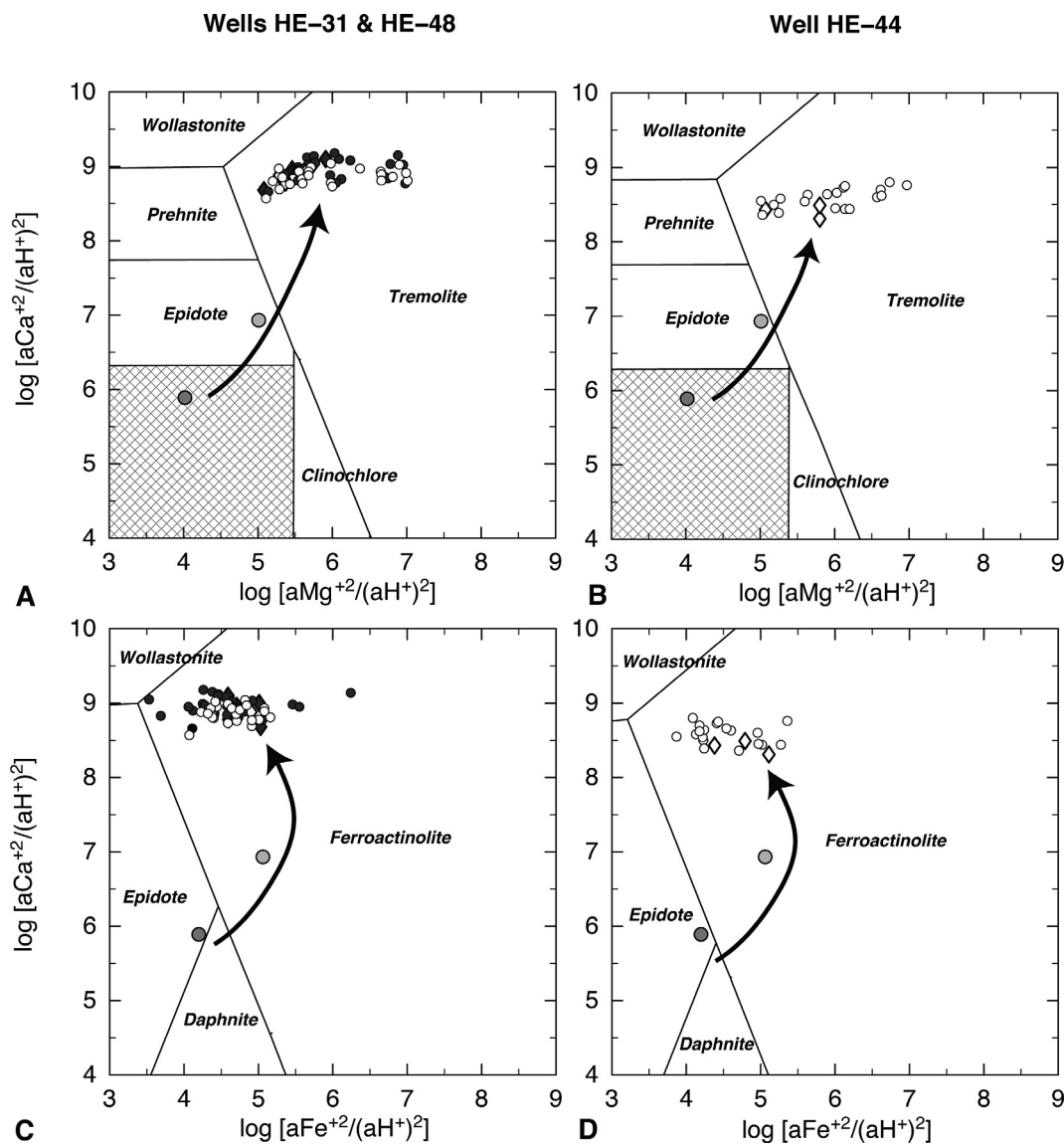
Wells HE–31 & HE–48   **Well HE–44**

Fig. 14. Predominance diagrams among some minerals in the CaO-MgO-FeO-Al$_2$O$_2$-SiO$_2$-H$_2$O system for monitoring wells (A) HE-31 and HE-48 at T = 266 °C, [Fe] = 0.482 µmol/kg, [Al] = 0.059 mmol/kg, and [Si] = 8.81 mmol/kg and (B) HE-44 at T = 277 °C, [Fe] = 0.444 µmol/kg, [Al] = 0.059 mmol/kg, and [Si] = 9.46 mmol/kg, and in the CaO-FeO-Al$_2$O$_2$-SiO$_2$-H$_2$O system for monitoring wells (C) HE-31 and HE-48 at T = 266 °C, [Al] = 0.064 mmol/kg, and [Si] = 8.81 mmol/kg and (D) HE-44 at T = 277 °C, [Al] = 0.059 mmol/kg, and [Si] = 9.46 mmol/kg. Black circles represent the in situ compositions of fluids collected from HE-31 and white circles the deep fluid from HE-48 and HE-44 with the black and white diamonds depicting the deep fluid pre-injection for each well. The gray circles represent the gas injected waters mixed with geothermal brine and heated to 260 °C (before any reaction in geothermal reservoir) with light gray symbols signifying the first two years of injection and the dark gray symbols after doubling the amount of injected gas. The cross-hatched area represents fluid compositions where no stable minerals are present. The temperature, [Si], [Al], and [Fe] are based on the average temperature and fluid compositions from HE-31, HE-48, and HE-44; wells HE-31 and HE-48 were grouped together because of their similar fluid compositions and same average temperature.

addition to fluorite precipitation, though the reservoir fluids were undersaturated with respect to fluorite (data not shown). Moreover, as there are trace amounts of phosphorus in basaltic glass (Oelkers and Gíslason, 2001) and Ca phosphate had been observed in CO$_2$-H$_2$S sequestration experiments by Marieni et al. (2018), phosphate minerals could also consume fluoride upon the dissolution of the basalt. Thus, the minor fluctuations in B, Cl$^-$, and F$^-$ concentrations could be attributed to dissolution of carbonate minerals already in the reservoir as the injected gas-charged

water plume moves towards the monitoring wells. Subsequent carbonate precipitation could then incorporate trace amounts of these anions.

6. IMPLICATIONS

6.1. Timescale of carbon and sulfur mineralization

At the original CarbFix site, where temperatures ranged from 20 to 50 °C and the acidity of the injected gases drove

mineral reactions, chemical equilibrium with most minerals was only attained after more than three months after CO_2 injection (Snæbjörnsdóttir et al., 2017). H_2S sequestration experiments reported by Přikryl et al. (2018) suggest that at higher temperatures (>200 °C) H_2S-fluid-mineral equilibrium is attained relatively fast compared to temperatures of ~100 °C. In this study, minerals such as calcite and iron sulfides attained equilibrium within the time it took for fluids to arrive at the first two monitoring wells, HE-31 and HE-48, as indicated by their saturation indices in Figs. 7 and 8. Thus the injected fluids attained equilibrium with respect to these minerals within one month in a > 250 °C geothermal reservoir. Furthermore, the stability of these minerals, in addition to the high temperature alteration minerals, epidote and actinolite, was not perturbed when gas injection switched from well HN-16 to HN-14 in July 2015 and when the amount of gas injected was doubled in July 2016.

Gunnarsson et al. (2018) reported that over 50% of the injected CO_2 and 76% of the injected H_2S were mineralized within a few months of continuous flow between the HN-16 injection well and the HE-31 first monitoring well, up to November 2015. This was based on mass balance calculations. Using the same approach, when the amount of injected gas was doubled in July 2016, we calculate that over 60% of injected CO_2 and over 85% of injected H_2S were mineralized within four months after the gas-charged waters were continuously injected into CarbFix2 site. This enhanced mineralization at CarbFix2, despite the decline in Ca concentrations, resulted from the increased acidity in the injected fluids and fewer secondary minerals reaching supersaturation (Clark et al., 2018) along with the increased water-rock interaction nearer to the monitoring wells (Table S-6). For comparison, mineralization of more than 95% of injected CO_2 was observed at the original CarbFix site and some of the injected supercritical CO_2 at the Wallula Basalt pilot site occurred within two years of injection (Matter et al., 2016; McGrail et al., 2017a, 2017b; Snæbjörnsdóttir et al., 2017).

This study thus further demonstrates the mineralization of carbon via the CarbFix method is faster by orders of magnitude than other common geological carbon storage methods. In the latter, CO_2 remains a separate phase for long periods of time in deep geological formations, such as depleted oil and gas reservoirs, coal formations, and saline formations. Over time, the injected CO_2 becomes less mobile through multiple trapping mechanisms, going from structural and stratigraphic trapping to solubility and mineral trapping (Benson and Cole, 2008). Mineral trapping of the injected CO_2 in such sedimentary basins, if it occurs, can take tens of thousands of years, limited by the low reactivity of silicate minerals in sedimentary rocks and the lack of Ca-, Mg-, and Fe-bearing minerals for carbonation (Gilfillan et al., 2009; Gislason and Oelkers, 2014).

6.2. Storage capacity

The total volume of mineral precipitation can be estimated by noting that one ton of CO_2 would create 0.84 m^3 of calcite and one ton of H_2S would create 0.70 m^3 of pyrite (Gunnarsson et al., 2018). If all the gas injected into the CarbFix2 site from June 2014 to December 2017 precipitated as calcite and pyrite, these minerals would have a total volume of about 29,000 m^3. As the target reservoir at Hellisheiði has a volume of 6×10^8 m^3, the precipitated calcite and pyrite would only consume 0.005 vol percent of the reservoir. If some of the available divalent cations were incorporated with the secondary minerals like epidote and actinolite instead of carbonates, these would still only take up less than 0.002 vol percent of the volume of the target basaltic reservoir (see Supplementary Material for further explanation). Overall, mineralization would constitute a relatively small volume compared to the reservoir size and thus likely negligibly affect its permeability. Note, however, that secondary mineral precipitation could create new fractures due to local pressure increases, thereby maintaining or enhancing the permeability (Jamtveit et al, 2009; Ulven et al., 2014). It is also likely that the relatively cold injection fluids (62 °C) compared to reservoir temperature (>250 °C), and the 9 bar overpressure at the well head, could result in thermal- and hydro-fracturing of the basalts near the injection well. Such possibilities are consistent with induced seismic activity (Gunnarsson et al., 2015b) and the observations that the permeability of the target reservoir systems has remained close to constant over the 3.5 year injection period.

Several estimates have been reported for the overall carbon and sulfur storage capacity of the 80 km^2 Hellisheiði geothermal reservoir. Sigfússon et al. (2018) estimated that the CO_2 storage potential of this reservoir ranges from 50 to 5200 Mt CO_2, although the average points towards the maximum estimate. A far smaller estimate of the storage potential of H_2S in this reservoir of 2.6 Mt H_2S was made based on the experiments of Přikryl et al. (2018). We estimate the storage capacities of 2430 Mt CO_2 and 1620 Mt H_2S based on the stoichiometry of Stapafell basaltic glass, and a geothermal reservoir extent of 80 km^2, assuming a storage formation of 0.1 km thick and 10% porosity. Considering Iceland emitted 7.1 Mt CO_2 in 2017, excluding agriculture, forestry, and other land use (Keller et al., 2019), and the country's geothermal energy sector emitted 19,000 tonnes H_2S in 2016 (Sigfússon et al., 2018), less than 2% of the storage potential at Hellisheiði would be consumed by storing all the CO_2 and H_2S emissions from Iceland each year. Furthermore, taking into account the distribution of natural carbon fixation in Iceland's geothermal systems, Snæbjörnsdóttir et al. (2014) estimated that 953–2470 Gt CO_2 could be stored in basaltic rocks in the active rift zones of Iceland, many orders of magnitude larger than Iceland's annual emissions. When taking into account the world's mid-oceanic basalt ridges, the storage capacity is on the order of 100,000–250,000 Gt CO_2 (Snæbjörnsdóttir et al., 2014). This storage potential is thus notably even larger than the 18,500 Gt CO_2 that can be attributed to the burning of all fossil fuel carbon on Earth (Archer, 2005), thereby highlighting that even with the substantial storage capacity within Iceland, the largest potential for CO_2 storage is offshore.

6.3. Temperature limitations for carbon and sulfur mineralization in meteoric water

Reaction path modelling of the low temperature (20–50 °C) CO_2 injection at the original CarbFix site indicates that the initial carbon mineralization might have begun with siderite precipitation at pH $\sim$ 5, then mixtures of Fe-, Mg-, and Ca-carbonates may form with increasing pH and decreasing pCO_2, followed by calcite at the highest pH and lowest pCO_2 (Snæbjörnsdóttir et al., 2018a). As the pH of the fluids collected from the original CarbFix monitoring well was >8, only calcite was observed in this well (Snæbjörnsdóttir et al., 2017). The increase in pCO_2 and Mg concentrations in the CarbFix2 monitoring well samples collected in the present study after doubling the gas injection rate in July 2016 forced the monitoring fluids into the dolomite's stability field (Fig. 7), suggesting greater fluid-rock interaction closer to the monitoring wells, and as previously mentioned, enhanced mineralization.

The temperature of the CarbFix2 target basaltic reservoir is close to that of the upper temperature limit of $\sim$280 °C for CO_2-H_2S mineral sequestration. Although the reservoir temperatures are stable and current DIC levels indicate calcite formation in Fig. 11A, injection at temperatures at 280 °C or higher would result in the precipitation of wollastonite rather than the mineralization of CO_2. The same applies to sulfide precipitation, as the fluids would favor epidote and magnetite precipitation at such temperatures (Fig. 11B). Nevertheless, the long-term success of the CarbFix2 subsurface mineralization testifies to the ability to store significant quantities of carbon and sulfur securely through mineral reactions from 20 °C up to $\sim$260 °C.

6.4. Alteration of basaltic crust

The results of this study demonstrate that the consumption of CO_2 by the dissolution of Ca-containing silicates in basaltic rocks coupled to calcite precipitation is rapid. Iceland is the largest part of the oceanic ridge system that is above sea level. From geological and surface water maps of Iceland, a relationship between the age of basalts and their decreasing permeability is evident. There is nearly no surface runoff within the rift zone. The number of streams and rivers noticeably increases outside of the Iceland's rift zone, which contains basalt rocks younger than 0.8 million years; the basalts surrounding this zone are not older than 3.3 million years (Gislason, 2008; Jóhannesson, 2014). Though this indicates a long timeframe for silicate weathering on the Earth's surface at ambient temperatures, it is an important sink for atmospheric CO_2 (Brady and Gislason, 1997; Gislason et al., 1996, 2009).

The low temperature (<60 °C) alteration of the oceanic crust from hydrothermal circulation is another important sink for CO_2 (Alt and Teagle, 1999; Brady and Gislason, 1997; Coogan and Gillis, 2018). Alteration of these basalts is considered to occur within 10–20 million years of its initial formation (Brady and Gislason, 1997; Coogan et al., 2016; Muehlenbachs, 1977), although they are already pervasively altered by 3.2 million years (Muehlenbachs, 1977; Muehlenbachs and Hodges, 1978).

The rapid formation of carbonates and silicates within the young and fractured basalts at the original CarbFix and CarbFix2 sites in Iceland suggests that such alteration reactions occur over timescales of months to years rather than millions of years, when the subsurface systems are perturbed by external forcing at 20 to $\sim$260 °C.

7. CONCLUSIONS

The results summarized above show that the carbon and sulfur mineralization at the CarbFix2 site in Hellisheiði, Iceland continue successfully and without slowing over the first 3.5 years of continued gas injection into this site. In fact, the efficiency of the mineralization has increased over time. During the first phase of injection, over 50% of injected carbon and 76% of sulfur mineralized within four to nine months according to mass balance calculations. These percentages increased, after the amount of gas injected was doubled; during the second phase of the injection over 60% of carbon and over 85% of sulfur were mineralized. The increased mineralization is likely due to the increased acidity of the injection fluid after the increase in gas concentration in the condensate water, resulting in enhanced dissolution in the vicinity of the injection well.

Notably, despite 3.5 years of injecting a CO_2-H_2S charged fluids for their mineralization into subsurface basaltic rock, there is no sign of a decrease in the permeability of the target reservoir. There are likely several reasons for this. First, the injection fluids are acidic and undersaturated with respect to the minerals present in the target reservoir. This will tend to open fluid pathways near the injection wells. Second, the volume of carbonate, sulfide, and other secondary minerals precipitating in the target aquifer was relatively small compared to the size of the reservoir (no more than a total of 0.025 volume percent of the target reservoir). Finally, new fractures may have formed as a result of pressure and temperature gradients close to the injection well induced by the injection of cooler gas-charged fluids.

Based on mineral saturation indices and predominance diagrams, the principal carbonates precipitating in the subsurface were calcite and potentially dolomite. Siderite was at saturation after the injected fluid was heated to >250 °C and therefore may be the first carbonate to reach saturation and potentially precipitate. Once the gas-charged injection fluids reached the monitoring wells, these fluids were saturated with respect to Ca-rich carbonates, typical for relatively low pCO_2 and high pH conditions (Clark et al., 2019; Rogers et al., 2006; Snæbjörnsdóttir et al., 2018a). A significant decrease in Ca concentrations was observed over time as DIC increased consistent with calcite saturation. As Ca and Mg concentrations were orders of magnitude lower than DIC, the release of these metals to the fluid phase likely limits carbonation in this system.

Declaration of Competing Interest

The authors declare that they have no known competing financial interests or personal relationships that could have appeared to influence the work reported in this paper.

APPENDIX A. SUPPLEMENTARY MATERIAL

Supplementary data to this article can be found online at https://doi.org/10.1016/j.gca.2020.03.039.

REFERENCES

Alfredsson H. A., Oelkers E. H., Hardarsson B. S., Franzson H., Gunnlaugsson E. and Gislason S. R. (2013) The geology and water chemistry of the Hellisheidi, SW-Iceland carbon storage site. *Int. J. Greenh. Gas Control* **12**, 399–418.

Alt J. C. and Teagle D. A. H. (1999) The uptake of carbon during alteration of ocean crust. *Geochim. Cosmochim. Acta* **63**, 1527–1535.

Aradóttir, E. S. P., Gunnarsson, I., Sigfusson, B., Gislason, S. R., Oelkers, E. H., Stute, M., Matter, J. M., Snæbjörnsdóttir, S. Ó., Mesfin, K., Alfredsson, H. A., Hall, J., Arnarson, M. T., Dideriksen, K., Júlíusson, B. M., Broecker, W. S. and Gunnlaugsson, E. (2015) Towards Cleaner Geothermal Energy: Subsurface Sequestration of Sour Gas Emissions from Geothermal Power Plants, World Geothermal Congress 2015, Melbourne, Australia.

Archer D. (2005) Fate of fossil fuel CO2 in geologic time. *J. Geophys. Res.* **110**, C09S05.

Arnorsson S., Bjarnason J. O., Giroud N., Gunnarsson I. and Stefansson A. (2006) Sampling and analysis of geothermal fluids. *Geofluids* **6**, 203–216.

Arnorsson S., Sigurdsson S. and Svavarsson H. (1982) The chemistry of geothermal waters in Iceland. I. Calculation of aqueous speciation from 0 °C to 370 °C. *Geochim. Cosmochim. Acta* **46**, 1513–1532.

Arnorsson S., Stefansson A. and Bjarnason J. O. (2007) Fluid-fluid interactions in geothermal systems. *Rev. Mineral. Geochem.* **65**, 259–312.

Arnórsson S., Axelsson G. and Sæmundsson K. (2008) Geothermal systems in Iceland. *Jökull* **58**, 269–302.

Benson S. M. and Cole D. R. (2008) CO2 sequestration in deep sedimentary formations. *Elements* **4**, 325–331.

Benson S. M. and Cook P. (2005) *Underground geological storage, IPCC Special Report on Carbon Dioxide Capture and Storage*. Cambridge University Press, Cambridge, U.K.

Bjarnason J. O. and Arnorsson S. (2010) The chemical speciation program. *WATCH* **2**(4), ed.

Brady P. V. and Gislason S. R. (1997) Seafloor weathering controls on atmospheric CO2 and global climate. *Geochim. Cosmochim. Acta* **61**, 965–973.

Clark D. E., Galeczka I., Dideriksen K., Voigt M., Wolff-Boenisch D. and Gislason S. (2019) Experimental observations of CO2-water-basaltic glass intereaction in a large column reactor experiment at 50°C. *Int. J. Greenh. Gas Control* **89**, 9–19.

Clark D. E., Gunnarsson I., Aradóttir E. S., Arnarson M. Þ., Þorgeirsson Þ. A., Sigurðardóttir S. S., Sigfússon B., Snæbjörnsdóttir S. Ó., Oelkers E. H. and Gíslason S. R. (2018) The chemistry and potential reactivity of the CO2-H2S charged injected waters at the basaltic CarbFix2 site, Iceland. *Energy Procedia* **146**, 121–128.

Coogan L. A. and Gillis K. M. (2018) Low-temperature alteration of the seafloor: impacts on ocean chemistry. *Ann. Rev. Earth Planet Sci* **46**, 21–45.

Coogan L. A., Parrish R. R. and Roberts N. M. W. (2016) Early hydrothermal carbon uptake by the upper oceanic crust: Insight from in situ U-Pb dating. *Geology* **44**, 147–150.

Fournier R. O. and Potter R. W. (1982) A revised and expanded silica (quartz) geothermometer. *GRC Bulletin*, 3–9.

Franzson H., Gunnlaugsson E., Árnason K., Sæmundsson K., Steingrímsson B. and Hardarsson B. S. (2010) *The Hengill Geothermal System, Conceptual Model and Thermal Evolution, World Geothermal Congress 2010, Bali, Indonesia*.

Franzson H., Kristjánsson B. R., Gunnarsson G., Björnsson G., Hjartarson A., Steingrímsson B., Gunnarsson E. and Gíslason G. (2005) *The Hengill-Hellisheiði Geothermal Field. Development of a Conceptual Geothermal Model, World Geothermal Congress 2005, Antalya, Turkey*.

Gilfillan S. M. V., Lollar V. S., Holland G., Blagburn D., Stevens S., Schoell M., Cassidy M., Ding Z., Zhou Z., Lacrampe-Couloume G. and Ballentine C. J. (2009) Solubility trapping in formation water as dominant CO2 sink in natural gas fields. *Nature* **458**, 614–618.

Gislason S. R. (2008) Weathering in Iceland. *Jökull* **58**, 387–408.

Gislason S. R. and Oelkers E. H. (2014) Carbon storage in basalt. *Science* **344**, 373–374.

Gislason S. R., Arnórsson S. and Ármannsson H. (1996) Chemical weathering of basalt in southwest Iceland: effects of runoff, age of rocks and vegetative/glacial cover. *Amer. J. Sci.* **296**, 837–907.

Gislason S. R., Oelkers E. H., Eiriksdottir E. S., Kardjilov M. I., Gisladottir G., Sigfusson B., Snorrason A., Elefson S., Hardardottir J., Torssander P. and Oskarsson N. (2009) Direct evidence of the feedback between climate and weathering. *Earth Planet. Sci. Lett.* **277**, 213–222.

Goldberg D., Aston L., Bonneville A., Demirkanli I., Evans C., Fisher A., Garcia H., Gerrard M., Heesemann M., Hnottavange-Telleen K., Hsu E., Malinverno C., Moran K., Park A.-H., Scherwath M., Slagle A., Stute M., Weathers T., Webb R., White M., White S. and the CarbonSAFE Cascadia Project Team (2018) Geological storage of CO2 in sub-seafloor basalt: the CarbonSAFE pre-feasibility study offshore Washington State and British Columbia. *Energy Procedia* **146**, 158–165.

Gunnarsson I., Aradóttir E. S., Oelkers E. H., Clark D. E., Arnarson M. Þ., Sigfússon B., Snæbjörnsdóttir S. Ó., Matter J. M., Stute M., Júlíusson B. M. and Gíslason S. R. (2018) The rapid and cost-effective capture and subsurface mineral storage of carbon and sulfur at the CarbFix2 site. *Int. J. Greenh. Gas Control* **79**, 117–126.

Gunnarsson I. and Arnorsson S. (2000) Amorphous silica solubility and the thermodynamic propoerties of H4SiO4 in the range of 0 to 350°C at Pamt. *Geochim. Cosmochim. Acta* **64**, 2295–2307.

Gunnarsson I., Júlíusson B. M., Aradóttir E. S., Sigfússon B. and Arnarson M. Þ. (2015a) *Pilot Scale Geothermal Gas Separation*. Hellisheiði Power Plant, Iceland, World Geothermal Congress, Melbourne, Australia.

Gunnarsson, G., Kristjánsson, B. R., Gunnarsson, I. and Júlíusson, B. M. (2015b) Reinjection into a Fractured Reservoir – Induced seismicity and other challenges in operating reinjection

wells in the Hellisheiði field, SW-Iceland, World Geothermal Congress 2015, Melbourne, Australia.

Hemming N. G., Reeder R. J. and Hanson G. N. (1995) Mineral-fluid partitioning and isotopic fractionation of boron in snythetic calcium carbonate. *Geochim. Cosmochim. Acta* **59**, 371–379.

Jamtveit B., Putnis C. V. and Malthe-Sørenssen A. (2009) Reaction induced fracturing during replacement processes. *Contrib. Mineral. Petr.* **157**, 127–133.

Jóhannesson H. (2014) *Geological Map of Iceland – Bedrock Geology – 1: 600 000*. Icelandic Institute of Natural History.

Keller, N., Stefani, M., Einarsdóttir, S. R., Helgadóttir, Á. K., Guðmundsson, J., Snorrason, A., Þórsson, J. and Tinganelli, L. (2019) National Inventory Report. The Environment Agency of Iceland.

Kinniburgh D. and Cooper D. (2011) *PhreePlot: Creating graphical output with PHREEQC*.

Kitano Y., Okumura M. and Idogaki M. (1975) Incorporation of sodium, chloride and sulfate with calcium carbonate. *Geochem. J.* **9**, 75–84.

Marieni C., Přikryl J., Aradóttir E. S., Gunnarsson I. and Stefánsson A. (2018) Towards 'green' geothermal energy: Co-mineralization of carbon and sulfur in geothermal reservoirs. *Int. J. Greenh. Gas Control* **77**, 96–105.

Matter J. M., Stute M., Snæbjörnsdóttir S. Ó., Oelkers E. H., Gíslason S. R., Aradóttir E. S., Sigfusson B., Gunnarsson I., Sigurdardóttir H., Gunnlaugsson E., Axelsson G., Alfredsson H. A., Wolff-Boenisch D., Mesfin K., de la Reguera Fernande, Taya D., Hall J., Dideriksen K. and Broecker W. S. (2016) Rapid carbon mineralization for permanent disposal of anthropogenic carbon dioxide emissions. *Science* **352**, 1312–1314.

McGrail B. P., Schaef H. T., Ho A. M., Chien Y.-J., Dooley J. J. and Davidson C. L. (2006) *Potential for carbon dioxide sequestration in flood basalts*. J. Geophys. Res. Solid Earth, p. 111.

McGrail B. P., Schaef H. T., Spane F. A., Cliff J. B., Qafoku O., Horner J. A., Thompson C. J., Owen A. T. and Sullivan C. E. (2017a) Field validation of supercritical CO_2 reactivity with basalts. *Environ. Sci. Tech. Let.* **4**, 6–10.

McGrail B. P., Schaef H. T., Spane F. A., Horner J. A., Owen A. T., Cliff J. B., Qafoku O., Thompson C. J. and Sullivan E. C. (2017b) Wallula basalt pilot demonstration project: post-injection results and conclusions. *Energy Procedia* **114**, 5783–5790.

Muhlenbachs K. (1977) Low temperature alteration oxygen isotope exchange between oceanic crust and seawater. *Proc. Symp. Water-Rock* **Interaction**, 317–326.

Muhlenbachs K. and Hodges F. N. (1978) Oxygen isotope geochemistry of rocks from DSDP leg 46. In *Initial Report of the Deep Sea Drilling Project (46)* (ed. L. Dmitriev). U.S. Gov't Print. Office, pp. 257–258.

Neveu M., Desch S. J. and Castillo-Rogez J. C. (2017) Aqueous geochemistry in icy world interiors: Equilibrium fluid, rock, and gas compositions, and fate of antifreezes and radionuclides. *Geochim. Cosmochim. Acta* **212**, 324–371.

Oelkers E. H., Butcher R., Pogge von Strandmann P. A. E., Schuessler J. A., von Blanckenburg F., Snæbjörnsdóttir S. Ó., Mesfin K., Aradóttir E. S., Gunnarsson I., Sigfússon B., Gunnlaugsson E., Matter J. M., Stute M. and Gislason S. R. (2019a) Using stable Mg isotope signatures to assess the fate of magnesium during the in situ mineralisation of CO_2 and H_2S at the CarbFix site in SW-Iceland. *Geochim. Cosmochim. Acta* **245**, 542–555.

Oelkers E. H. and Gislason S. R. (2001) The mechanism, rates and consequences of basaltic glass dissolution: I. An experimental study of the dissolution rates of basaltic glass as a function of aqueous Al, Si and oxalic acid concentration at 25°C and pH = 3 and 11. *Geochim. Cosmochim. Acta* **65**, 3671–3681.

Oelkers E. H., Pogge von Strandmann P. A. E. and Mavromatis V. (2019b) The rapid resetting of the Ca isotope signatures of calcite at ambient temperature during its congruent dissolution, precipitation, and at equilibrium. *Chem. Geol.* **512**, 1–10.

Parkhurst D. L. and Appelo C. A. J. (2013) Description of Input and Examples for PHREEQC Version 3 – A Computer Program for Speciation, Batch-Reaction, One-Dimensional Transport, and Inverse Geochemical Calculations. In *Techniques and Methods* (ed. U. S. G. Survey), p. 497.

Pogge von Strandmann P. A. E., Burton K. W., Snaebjornsdottir S. O., Sigfusson B., Aradottir E. S., Gunnarsson I., Alfredsson H. A., Mesfin K. G., Oelkers E. H. and Gislason S. R. (2019) Rapid CO_2 mineralisation into calcite at the CarbFix storage site quantified using calcium isotopes. *Nat. Commun.* **10**, 1983.

Power I. M., Harrison A. L., Dipple G. M., Wilson S. A., Kelemen P. B., Hitch M. and Southam G. (2013) Carbon mineralization: from natural analogues to engineered systems. *Rev. Mineral. Geochem.* **77**, 305–360.

Přikryl J., Marieni C., Gudbrandsson S., Aradóttir E. S., Gunnarsson I. and Stefánsson A. (2018) H_2S sequestration process and sustainability in geothermal systems. *Geothermics* **71**, 156–166.

Rogers K. L., Neuhoff P. S., Pedersen A. K. and Bird D. K. (2006) CO_2 metasomatism in a basalt-hosted petroleum reservoir, Nuussuaq, West Greenland. *Lithos* **92**, 55–82.

Saldi G. D., Noireaux J., Louvat P., Faure L., Balan E., Schott J. and Gaillardet J. (2018) Boron isotopic fractionation during adsorption by calcite – Implication for the seawater pH proxy. *Geochim. Cosmochim. Acta* **240**, 255–273.

Sigfússon B., Arnarson M. Þ., Snæbjörnsdóttir S. Ó., Karlsdóttir M. R., Aradóttir E. S. and Gunnarsson I. (2018) Reducing emissions of carbon dioxide and hydrogen sulphide at Hellisheidi power plant in 2014–2017 and the role of CarbFix in achieving the 2040 Iceland climate goals. *Energy Procedia* **146**, 135–145.

Sigfusson B., Gislason S. R., Matter J. M., Stute M., Gunnlaugsson E., Gunnarsson I., Aradottir E. S., Sigurdardottir H., Mesfin K., Alfredsson H. A., Wolff-Boenisch D., Arnarsson M. T. and Oelkers E. H. (2015) Solving the carbon-dioxide buoyancy challenge: the design and field testing of a dissolved CO_2 injection system. *Int. J. Greenh. Gas Control* **37**, 213–219.

Skippen G. B. (1977) Dehydration and decarbonation equilibria. In *Application of Thermodynamics to Petrology and Ore Deposits. Short Course*, Vol. 2 (ed. H. J. Greenwood). Mineralogical Association of Canada. Evergreen Press Limited, Vancouver.

Snæbjörnsdóttir S. Ó., Gislason S. R., Galeczka I. M. and Oelkers E. H. (2018a) Reaction path modelling of in-situ mineralisation of CO_2 at the CarbFix site at Hellisheidi, SW-Iceland. *Geochim. Cosmochim. Acta* **220**, 348–366.

Snæbjörnsdóttir S. Ó., Oelkers E. H., Mesfin K., Aradóttir E. S., Dideriksen K., Gunnarsson I., Gunnlaugsson E., Matter J. M., Stute M. and Gislason S. R. (2017) The chemistry and saturation states of subsurface fluids during the in situ mineralisation of CO_2 and H_2S at the CarbFix site in SW-Iceland. *Int. J. Greenh. Gas Control* **58**, 87–102.

Snæbjörnsdóttir S. Ó., Tómasdóttir S., Sigfússon B., Aradottir E. S., Gunnarsson G., Niemi A., Basirat F., Dessirier B., Gislason S. R., Oelkers E. H. and Franzson H. (2018b) The geology and hydrology of the CarbFix2 site, SW-Iceland. *Energy Procedia* **146**, 146–157.

Snæbjörnsdóttir S. Ó., Wiese F., Fridriksson T., Ármansson H., Einarsson G. M. and Gislason S. R. (2014) CO_2 storage potential of basaltic rocks in Iceland and the oceanic ridges. *Energy Procedia* **63**, 4585–4600.

Stefánsson A., Arnórsson S., Gunnarsson I., Kaasalainen H. and Gunnlaugsson E. (2011) The geochemistry and sequestration of H$_2$S into the geothermal system at Hellisheidi, Iceland. *J. Volcanol. Geoth. Res.* **202**, 179–188.

Tómasdóttir S. (2018) *Flow Paths in the Húsmúli Reinjection Zone, Iceland, Department of Earth Sciences* MSc Thesis. Uppsala University, Uppsala, Sweden.

Turner B. D., Binning P. and Stipp S. L. S. (2005) Fluoride removal by calcite: evidence for fluorite precipitation and surface adsorption. *Environ. Sci. Technol.* **39**, 9561–9568.

Ulven O. I., Jamveit B. and Malthe-Sørenssen A. (2014) Reaction-driven fracturing of porous rocks. *J. Geophys. Res. Solid Earth* **119**, 7473–7485.

Voigt M., Marieni C., Clark D. E., Gislason S. R. and Oelkers E. H. (2018a) Evaluation and refinement of thermodynamic databases for mineral carbonation. *Energy Procedia* **146**, 81–91.

Voigt M., Pearce C. R., Baldermann A. and Oelkers E. H. (2018b) Stable and radiogenic strontium isotope fractionation during hydrothermal seawater-basalt interaction. *Geochim. Cosmochim. Acta* **240**, 131–151.

Associate editor: Chen Zhu